

1 **ELASTIC WAVE PROPAGATION IN CURVILINEAR COORDINATES WITH MESH
2 REFINEMENT INTERFACES BY A FOURTH ORDER FINITE DIFFERENCE
3 METHOD**

4 LU ZHANG*, SIYANG WANG†, AND N. ANDERS PETERSSON‡

5 **Abstract.** We develop a fourth order accurate finite difference method for the three dimensional elastic wave equation
6 in isotropic media with the piecewise smooth material property. In our model, the material property can be discontinuous at
7 curved interfaces. The governing equations are discretized in second order form on curvilinear meshes by using a fourth order
8 finite difference operator satisfying a summation-by-parts property. The method is energy stable and high order accurate.
9 The highlight is that mesh sizes can be chosen according to the velocity structure of the material so that computational
10 efficiency is improved. At the mesh refinement interfaces with hanging nodes, physical interface conditions are imposed
11 by using ghost points and interpolation. With a fourth order predictor-corrector time integrator, the fully discrete scheme
12 is energy conserving. Numerical experiments are presented to verify the fourth order convergence rate and the energy
13 conserving property.

14 **Key words.** Elastic wave equations, Three space dimension, Finite difference methods, Summation-by-parts, Non-
15 conforming mesh refinement

16 **AMS subject classifications.** 65M06, 65M12

17 **1. Introduction.** Seismic wave propagation has important applications in earthquake simulation,
18 energy resources exploration, and underground motion analysis. In many practical problems, wave motion
19 is governed by the three dimensional (3D) anisotropic elastic wave equations. The layered structure of
20 the Earth gives rise to a piecewise smooth material property with discontinuities at internal interfaces,
21 which are often curved in realistic models. Because of the heterogeneous material property and internal
22 interfaces, the governing equations cannot be solved analytically, and it is necessary to use advanced
23 numerical techniques to solve the seismic wave propagation problem.

24 When solving hyperbolic partial differential equations (PDEs), for computational efficiency, it is
25 essential that the numerical methods are high order accurate (higher than second order). This is because
26 high order methods have much smaller dispersion error than lower order methods [7, 9]. However, it is
27 challenging to obtain a stable and high order accurate method in the presence of discontinuous material
28 property and non-trivial geometry.

29 Traditionally, the governing equations of seismic wave propagation are solved as a first order system,
30 either in velocity-strain or velocity-stress formulation, which consists of nine equations. With the finite
31 difference method, staggered grids are often used for first order systems, and recently the technique has
32 been generalized to staggered curvilinear grids for the wave equation [13]. The finite difference method
33 on non-staggered grids has also been developed for seismic wave simulation in 2D [8] and 3D [5].

34 In this paper, we use another approach that discretizes the governing equations in second order form.
35 Comparing with nine PDEs in a first order system, the second order formulation consists of only three
36 PDEs in the displacement variables. In many cases, this could be a more efficient approach in terms
37 of accuracy and memory usage. For spatial discretization, we consider the finite difference operators
38 constructed in [16] that satisfy a summation-by-parts (SBP) principle, which is a discrete analog of
39 the integration-by-parts principle and is an important ingredient to obtain energy stability. The SBP
40 operators in [16] use a ghost point outside each boundary to impose boundary conditions strongly. The
41 ghost point values are obtained by solving a system of linear equations. This can be avoided by imposing
42 boundary conditions in a weak sense [2] with the SBP operators constructed in [12] that do not use any
43 ghost point. The close relationship between these two types of SBP operators is explored in [21], where
44 it was also shown in test problems that the approach using ghost points has better CFL property.

45 In the SBP finite difference framework, a multi-block approach is often taken when the material

*Department of Applied Physics and Applied Mathematics, Columbia University, New York, NY 10027, USA. Email:
lz2784@columbia.edu

†Division of Applied Mathematics, UKK, Mälardalen University, Västerås, Sweden. Email: siyang.wang@mdh.se

‡Center for Applied Scientific Computing, Lawrence Livermore National Laboratory, Livermore, CA 94551, USA. Email:
petersson1@llnl.gov

46 property is discontinuous. That is, the domain is divided into subdomains such that the internal interfaces
 47 are aligned with the material discontinuities. Each subdomain has four sides in 2D and six faces in 3D,
 48 which can then be mapped to a reference domain, for example, a unit square in 2D and a unit cube in
 49 3D. In each subdomain, material properties are smooth and SBP operators are used independently for
 50 the spatial discretization of the governing equations. To patch subdomains together, physical interface
 51 conditions are imposed at internal interfaces [1, 6]. It is challenging to derive energy stable interface
 52 coupling with high order accuracy.

53 In [14], a fourth order SBP finite difference method was developed to solve the 3D elastic wave
 54 equation in heterogeneous smooth media, where topography in non-rectangular domains is resolved by
 55 using curvilinear meshes. The main objective of the present paper is to develop a fourth order method
 56 that solves the governing equations in piecewise smooth media, where material discontinuities occur at
 57 curved interfaces. This is motivated by the fact that in realistic models, material properties are only
 58 piecewise smooth with discontinuities, and it is important to obtain high order accuracy even at the
 59 material interfaces. A highlight of our method is that mesh sizes in each subdomain can be chosen
 60 according to the velocity structure of the material property. This leads to difficulties in mesh refinement
 61 interfaces, but maximizes computational efficiency. In the context of seismic wave propagation, as going
 62 deeper in the Earth, the wave speed gets larger and the wavelength gets longer. Correspondingly, in
 63 our model, the mesh becomes coarser with increasing depth. In this way, the number of grid points per
 64 wavelength can be kept almost the same in the entire domain. In addition, curved interfaces are also
 65 useful when the top surface has a very complicated geometry. If only planar interfaces are used [15],
 66 the size of the finest mesh block on top must be large to keep small skewness of the grid. With curved
 67 interfaces, the size of the finest mesh block can be reduced without increasing the skewness of the grid.

68 In [21], we developed a fourth order finite difference method for the 2D wave equations with mesh
 69 refinement interfaces on Cartesian grids. Our current work generalizes to 3D elastic wave equations on
 70 curvilinear grids. In a 3D domain, the material interfaces are 2D curved faces. To impose interface
 71 conditions on hanging nodes, we construct fourth order interpolation and restriction operators for 2D
 72 grid functions. These operators are compatible with the underlying finite difference operators. With a
 73 fourth order predictor-corrector time integrator, the fully discrete discretization is energy conserving.

74 The rest of the paper is organized as follows. In Sec. 2, we introduce the governing equations in
 75 curvilinear coordinates. The spatial discretization is presented in detail in Sec. 3. Particular emphasis is
 76 placed on the numerical coupling procedure at curved mesh refinement interfaces. In Sec. 4, we describe
 77 the temporal discretization and present the fully discrete scheme. Numerical experiments are presented in
 78 Sec. 5 to verify the convergence rate of the proposed scheme and the energy conserving property. We also
 79 demonstrate that the mesh refinement interfaces do not introduce spurious wave reflections. Conclusions
 80 are drawn in Sec. 6.

81 **2. The anisotropic elastic wave equation.** We consider the time dependent anisotropic elastic
 82 wave equation in a three dimensional domain $\mathbf{x} \in \Omega$, where $\mathbf{x} = (x^{(1)}, x^{(2)}, x^{(3)})^T$ are the Cartesian
 83 coordinates. The domain Ω is partitioned into two subdomains Ω^f and Ω^c , with an interface $\Gamma = \Omega^f \cap \Omega^c$.
 84 The material property is assumed to be smooth in each subdomain, but may be discontinuous at the
 85 interface Γ . Without loss of generality, we may assume that the wave speed is slower in Ω^f than in
 86 Ω^c , which motivates us to use a fine mesh in Ω^f and a coarse mesh in Ω^c . We further assume that
 87 both Ω^f and Ω^c have six, possibly curved boundary faces. Denote $\mathbf{r} = (r^{(1)}, r^{(2)}, r^{(3)})^T$, the parameter
 88 coordinates, and introduce smooth one-to-one mappings

89 (2.1)
$$\mathbf{x} = \mathbf{X}^f(\mathbf{r}) : [0, 1]^3 \rightarrow \Omega^f \subset \mathbb{R}^3 \quad \text{and} \quad \mathbf{x} = \mathbf{X}^c(\mathbf{r}) : [0, 1]^3 \rightarrow \Omega^c \subset \mathbb{R}^3.$$

90 Let the inverse of the mappings in (2.1) be $\mathbf{r} = \mathbf{R}^f(\mathbf{x})$ with components $\mathbf{R}^f(\mathbf{x}) = (R^{f,(1)}, R^{f,(2)}, R^{f,(3)})^T$
 91 and $\mathbf{r} = \mathbf{R}^c(\mathbf{x})$ with components $\mathbf{R}^c(\mathbf{x}) = (R^{c,(1)}, R^{c,(2)}, R^{c,(3)})^T$, respectively. Note that we do not
 92 compute the components of the inverse mapping \mathbf{R}^c and \mathbf{R}^f in this paper, the definitions here are for
 93 the convenience of the rest of the contents.

94 We further assume that the interface Γ corresponds to $r^{(3)} = 1$ for the coarse domain and $r^{(3)} = 0$
 95 for the fine domain. Then the elastic wave equation in the coarse domain Ω^c in terms of the displacement

96 vector $\mathbf{C} = \mathbf{C}(\mathbf{r}, t)$ can be written in curvilinear coordinates as (see [14])

97 (2.2)
$$\rho^c \frac{\partial^2 \mathbf{C}}{\partial^2 t} = \frac{1}{J^c} [\bar{\partial}_1(A_1^c \nabla_r \mathbf{C}) + \bar{\partial}_2(A_2^c \nabla_r \mathbf{C}) + \bar{\partial}_3(A_3^c \nabla_r \mathbf{C})], \quad \mathbf{r} \in [0, 1]^3, \quad t \geq 0,$$

99 where ρ^c is the density function in the coarse domain Ω^c . We define

100
$$A_k^c \nabla_r \mathbf{C} = \sum_{j=1}^3 N_{kj}^c \bar{\partial}_j \mathbf{C}, \quad k = 1, 2, 3,$$

102 with $\nabla_r = (\bar{\partial}_1, \bar{\partial}_2, \bar{\partial}_3)^T$, $\bar{\partial}_i = \frac{\partial}{\partial r^{(i)}}$, for $i = 1, 2, 3$ and

103 (2.3)
$$N_{ij}^c = J^c \sum_{l,k=1}^3 \xi_{li}^c O_l^T Q^c O_k \xi_{kj}^c, \quad i, j = 1, 2, 3,$$

104 where,

105
$$O_1^T = \begin{pmatrix} 1 & 0 & 0 & 0 & 0 & 0 \\ 0 & 0 & 0 & 0 & 0 & 1 \\ 0 & 0 & 0 & 0 & 1 & 0 \end{pmatrix}, \quad O_2^T = \begin{pmatrix} 0 & 0 & 0 & 0 & 0 & 1 \\ 0 & 1 & 0 & 0 & 0 & 0 \\ 0 & 0 & 0 & 1 & 0 & 0 \end{pmatrix}, \quad O_3^T = \begin{pmatrix} 0 & 0 & 0 & 0 & 1 & 0 \\ 0 & 0 & 0 & 1 & 0 & 0 \\ 0 & 0 & 1 & 0 & 0 & 0 \end{pmatrix},$$

106 Q^c is a 6×6 stiffness matrices which is symmetric and positive definite and $\xi_{kj} = \frac{\partial r^{(j)}}{\partial x^{(k)}}$. Further, Define
107 $M_{lk}^c = O_l^T Q O_k$, then M_{ii}^c are also symmetric positive definite and $M_{ij}^c = M_{ji}^T$. In particular, for the
108 isotropic elastic wave equation, we have

109
$$M_{11}^c = \begin{pmatrix} 2\mu^c + \lambda^c & 0 & 0 \\ 0 & \mu^c & 0 \\ 0 & 0 & \mu^c \end{pmatrix}, \quad M_{12}^c = \begin{pmatrix} 0 & \lambda^c & 0 \\ \mu^c & 0 & 0 \\ 0 & 0 & 0 \end{pmatrix},$$

110

111 (2.4)
$$M_{22}^c = \begin{pmatrix} \mu^c & 0 & 0 \\ 0 & 2\mu^c + \lambda^c & 0 \\ 0 & 0 & \mu^c \end{pmatrix}, \quad M_{13}^c = \begin{pmatrix} 0 & 0 & \lambda^c \\ 0 & 0 & 0 \\ \mu^c & 0 & 0 \end{pmatrix},$$

112

113
$$M_{33}^c = \begin{pmatrix} \mu^c & 0 & 0 \\ 0 & \mu^c & 0 \\ 0 & 0 & 2\mu^c + \lambda^c \end{pmatrix}, \quad M_{23}^c = \begin{pmatrix} 0 & 0 & 0 \\ 0 & 0 & \lambda^c \\ 0 & \mu^c & 0 \end{pmatrix},$$

114

115
$$M_{31}^c = (M_{13}^c)^T, \quad M_{32}^c = (M_{23}^c)^T, \quad M_{21}^c = (M_{12}^c)^T.$$

116 Here, λ^c and μ^c are the first and second Lamé parameters, respectively.

117 From (2.3) we find that even in the isotropic case the matrices N_{ij}^c are full. Hence, wave propagation
118 in isotropic media has anisotropic properties in curvilinear coordinates. In both isotropic and anisotropic
119 material, the matrices N_{ii}^c , $i = 1, 2, 3$, are symmetric positive definite and $N_{ij}^c = (N_{ji}^c)^T$, $i, j = 1, 2, 3$.

120 Last, J^c is the Jacobian of the coordinate transformation with

121
$$J^c = \det(\bar{\partial}_1 \mathbf{X}^c, \bar{\partial}_2 \mathbf{X}^c, \bar{\partial}_3 \mathbf{X}^c) \in (0, \infty).$$

122 Denote the unit outward normal $\mathbf{n}_i^{c,\pm} = (n_i^{c,\pm,1}, n_i^{c,\pm,2}, n_i^{c,\pm,3})$, $i = 1, 2, 3$, for the boundaries of the
123 subdomain Ω^c , then

124 (2.5)
$$\mathbf{n}_i^{c,\pm} = \pm \frac{\nabla_x R^{c,(i)}}{|\nabla_x R^{c,(i)}|}.$$

125

126 Here, $\nabla_x = (\partial_1, \partial_2, \partial_3)^T$, $\partial_i = \frac{\partial}{\partial x^{(i)}}$, $i = 1, 2, 3$. Here, '+' corresponds to $r^{(i)} = 1$ and '-' corresponds
127 to $r^{(i)} = 0$. The relation between covariant basis vectors $\bar{\partial}_i \mathbf{X}^c$, $i = 1, 2, 3$ and contravariant basis vectors

128 $\nabla_x R^{c,(i)}, i = 1, 2, 3$ can be found in [14, 18]. The elastic wave equation in curvilinear coordinates for the
 129 fine domain in terms of the displacement vector $\mathbf{F} = \mathbf{F}(\mathbf{r}, t)$ is defined in the same way as in the coarse
 130 domain. We have

$$131 \quad (2.6) \quad \rho^f \frac{\partial^2 \mathbf{F}}{\partial^2 t} = \frac{1}{J^f} \left[\bar{\partial}_1(A_1^f \nabla_r \mathbf{F}) + \bar{\partial}_2(A_2^f \nabla_r \mathbf{F}) + \bar{\partial}_3(A_3^f \nabla_r \mathbf{F}) \right], \quad \mathbf{r} \in [0, 1]^3, \quad t \geq 0.$$

133 At the interface Γ , suitable physical interface conditions are the continuity of the traction vectors
 134 and the continuity of the displacement vectors,

$$135 \quad (2.7) \quad \frac{A_3^c \nabla_r \mathbf{C}}{J^c \Lambda^c} = \frac{A_3^f \nabla_r \mathbf{F}}{J^f \Lambda^f}, \quad \mathbf{F} = \mathbf{C},$$

136 where

$$137 \quad (2.8) \quad \Lambda^c = |\nabla_x R^{c,(3)}|, \quad \Lambda^f = |\nabla_x R^{f,(3)}|.$$

138 Together with suitable physical boundary conditions, the problem (2.2, 2.6) is well-posed [6, 14].

139 **3. The spatial discretization.** In this section, we describe the spatial discretization for the prob-
 140 lem (2.2, 2.6, 2.7) and start with the SBP operators for the first and second derivative.

141 **3.1. SBP operators in 1D.** Consider a uniform discretization of the domain $x \in [0, 1]$ with the
 142 grids,

$$143 \quad \tilde{\mathbf{x}} = [x_0, x_1, \dots, x_n, x_{n+1}]^T, \quad x_i = (i-1)h, \quad i = 0, 1, \dots, n, n+1, \quad h = 1/(n-1),$$

144 where $i = 1, n$ correspond to the grid points at the boundary, and $i = 0, n+1$ are ghost points outside
 145 of the physical domain. The operator $D \approx \frac{\partial}{\partial x}$ is a first derivative SBP operator [10, 17] if

$$146 \quad (3.1) \quad (\mathbf{u}, D\mathbf{v})_h = -(D\mathbf{u}, \mathbf{v})_h - u_1 v_1 + u_n v_n,$$

147 with a scalar product

$$148 \quad (3.2) \quad (\mathbf{u}, \mathbf{v})_h = h \sum_{i=1}^n \omega_i u_i v_i.$$

149 Here, $0 < \omega_i < \infty$ are the weights of scalar product. The SBP operator D has a centered difference stencil
 150 at the grid points away from the boundary and the corresponding weights $\omega_i = 1$. To satisfy the SBP
 151 identity (3.1), the coefficients in D are modified at a few points near the boundary and the corresponding
 152 weights $\omega_i \neq 1$. The operator D does not use any ghost points. To discretize the elastic wave equation,
 153 we also need to approximate the second derivative with a variable coefficient $(\gamma(x)u_x)_x$. Here, the known
 154 function $\gamma(x) > 0$ describes the property of the material. There are two different fourth order accurate
 155 SBP operators for the approximation of $(\gamma(x)u_x)_x$. The first one $\tilde{G}(\gamma)\mathbf{u} \approx (\gamma(x)u_x)_x$, derived by Sjögren
 156 and Petersson [16], uses one ghost point outside each boundary, and satisfies the second derivative SBP
 157 identity,

$$158 \quad (3.3) \quad (\mathbf{u}, \tilde{G}(\gamma)\mathbf{v})_h = -S_\gamma(\mathbf{u}, \mathbf{v}) - u_1 \gamma_1 \tilde{\mathbf{b}}_1 \mathbf{v} + u_n \gamma_n \tilde{\mathbf{b}}_n \mathbf{v}.$$

159 Here, the symmetric positive semi-definite bilinear form $S_\gamma(\mathbf{u}, \mathbf{v}) = (Du, \gamma Dv)_h + (\mathbf{u}, P(\gamma)\mathbf{v})_{hr}$ does not
 160 use any ghost points, $(\cdot, \cdot)_{hr}$ is a standard discrete scalar L^2 inner product. The positive semi-definite
 161 operator $P(\gamma)$ is small for smooth grid functions but non-zero for odd-even modes, see [14, 16] for details.
 162 The operators $\tilde{\mathbf{b}}_1$ and $\tilde{\mathbf{b}}_n$ take the form

$$163 \quad (3.4) \quad \tilde{\mathbf{b}}_1 \mathbf{v} = \frac{1}{h} \sum_{i=0}^4 \tilde{d}_i v_i, \quad \tilde{\mathbf{b}}_n \mathbf{v} = \frac{1}{h} \sum_{i=n-3}^{n+1} \tilde{d}_i v_i.$$

164 They are fourth order approximations of the first derivative v_x on the left and right boundaries, respec-
 165 tively. We note that the notation $\tilde{G}(\gamma)\mathbf{v}$ implies that the operator \tilde{G} uses \mathbf{v} on all grid points $\tilde{\mathbf{x}}$, but

166 $\tilde{G}(\gamma)\mathbf{v}$ only returns values on the grid \mathbf{x} without ghost points. Therefore, when writing in matrix form,
 167 \tilde{G} is a rectangular matrix of size n by $n + 2$.

168 In [21], a method was developed to convert the SBP operator $\tilde{G}(\gamma)$ to another SBP operator $G(\gamma)$
 169 which does not use any ghost point and satisfy

170 (3.5)
$$(\mathbf{u}, G(\gamma)\mathbf{v})_h = -S_\gamma(\mathbf{u}, \mathbf{v}) - u_1\gamma_1\mathbf{b}_1\mathbf{v} + u_n\gamma_n\mathbf{b}_n\mathbf{v},$$

171 where $S_\gamma(\cdot, \cdot)$ is symmetric positive semi-definite. Here, \mathbf{b}_1 and \mathbf{b}_n are also finite difference operators for
 172 the first derivative at the boundaries, and are constructed to fourth order accuracy. They take the form

173 (3.6)
$$\mathbf{b}_1\mathbf{v} = \frac{1}{h} \sum_{i=1}^5 d_i v_i, \quad \mathbf{b}_n\mathbf{v} = \frac{1}{h} \sum_{i=n-4}^n d_i v_i.$$

174 In this case, $G(\gamma)$ is square in matrix form. We note that in [12], Mattsson constructed a similar SBP
 175 operator with a third order approximation of the first derivative at the boundaries.

176 For the second derivative SBP operators $\tilde{G}(\gamma)$ in (3.3) and $G(\gamma)$ in (3.5), both of them use a fourth
 177 order five points centered difference stencil to approximate $(\gamma u_x)_x$ at the interior points away from the
 178 boundaries. For the first and the last six grid points close to the boundaries, the operators $G(\gamma)$ and
 179 $\tilde{G}(\gamma)$ use second order accurate one-sided difference stencils. They are designed to satisfy (3.5) and (3.3),
 180 respectively.

181 In the following section, we use a combination of two SBP operators, $\tilde{G}(\gamma)$ and $G(\gamma)$, to develop a
 182 multi-block finite difference discretization for the elastic wave equation. The first SBP operator is $\tilde{G}(\gamma)$
 183 with ghost point, and the second SBP operator $G(\gamma)$, converted from $\tilde{G}(\gamma)$, does not use ghost point.

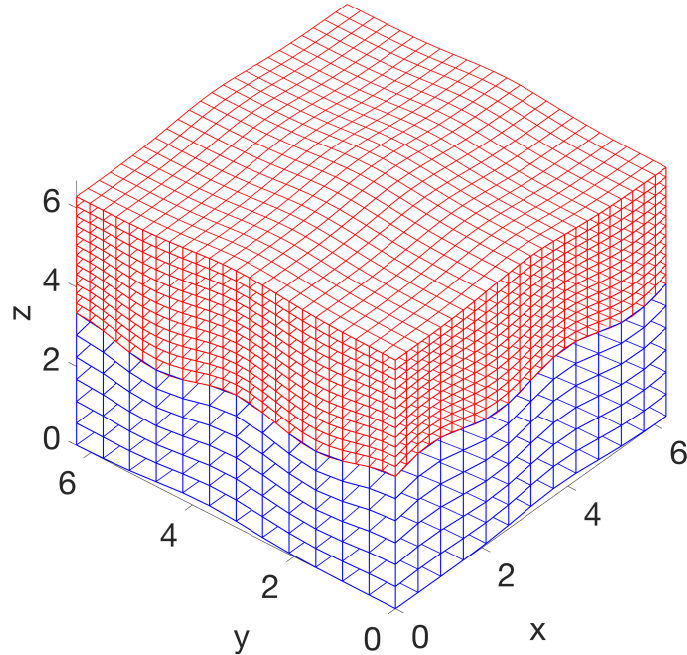


FIG. 1. The sketch for the curvilinear mesh of the physical domain Ω . The blue region is the spatial discretization of coarse subdomain Ω^c and the red region is the spatial discretization of the fine domain Ω^f . Note that x, y, z in the graph correspond to $x^{(1)}, x^{(2)}, x^{(3)}$ respectively.

184 **3.2. Semi-discretization of the elastic wave equation.** In this section, we discretize the elastic
 185 wave equations (2.2) and (2.6) with mesh refinement interface Γ . We assume the ratio of mesh sizes in

186 the reference domains is $1 : 2$, that is the mesh sizes satisfy

$$187 \quad h_1(n_1^h - 1) = 1, \quad h_2(n_2^h - 1) = 1, \quad h_3(n_3^h - 1) = 1,$$

188 and

$$189 \quad 2h_1(n_1^{2h} - 1) = 1, \quad 2h_2(n_2^{2h} - 1) = 1, \quad 2h_3(n_3^{2h} - 1) = 1.$$

190 Other ratios can be treated analogously. Figure 1 gives an illustration of the discretization of a physical
191 domain. This is an ideal mesh if the wave speed in Ω^f is half of the wave speed in Ω^c .

192 In seismic wave simulation, far-field boundary conditions are often imposed in the $x^{(1)}$ and $x^{(2)}$
193 directions. Here, our focus is on the numerical treatment of the interface conditions (2.7). Therefore, we
194 assume periodic boundary conditions in $x^{(1)}$ and $x^{(2)}$ and ignore the boundaries in $x^{(3)}$. In Figure 2, we
195 fix $x^{(2)} = 0$ and present the $x^{(1)}\text{-}x^{(3)}$ section of the domain Ω in both curvilinear space and parameter
space. To condense notations, we introduce the multi-index notations

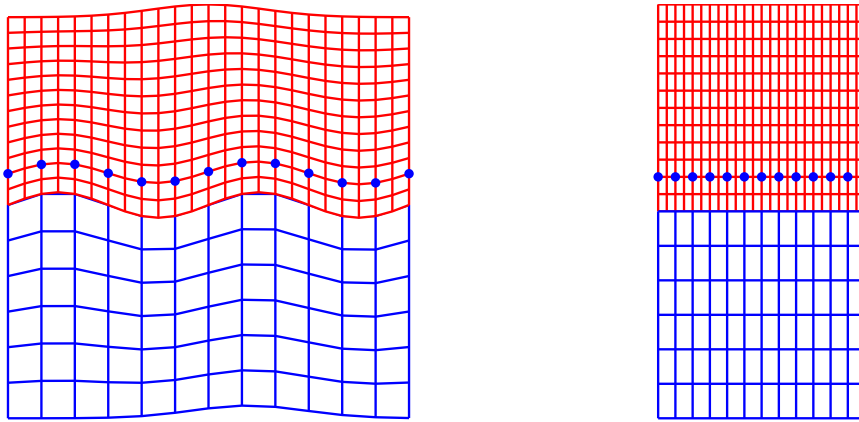


FIG. 2. The meshes in the physical domain (left) and parameter domain (right) of $x^{(1)}\text{-}x^{(3)}$ section with $x^{(2)} = 0$.
The blue dots are the ghost points for the coarse domain Ω^c .

196

$$197 \quad \mathbf{i} = (i, j, k), \quad \mathbf{r}_i = (r_i^{(1)}, r_j^{(2)}, r_k^{(3)}), \quad \mathbf{x}_i = (x_i^{(1)}, x_j^{(2)}, x_k^{(3)}),$$

198 and group different sets of grid points according to

$$\begin{aligned} I_{\Omega^c} &= \{i = 1, 2, \dots, n_1^{2h}, j = 1, 2, \dots, n_2^{2h}, k = 1, 2, \dots, n_3^{2h}\}, \\ I_{\Gamma^c} &= \{i = 1, 2, \dots, n_1^{2h}, j = 1, 2, \dots, n_2^{2h}, k = n_3^{2h}\}, \\ I_{\Omega^f} &= \{i = 1, 2, \dots, n_1^h, j = 1, 2, \dots, n_2^h, k = 1, 2, \dots, n_3^h\}, \\ I_{\Gamma^f} &= \{i = 1, 2, \dots, n_1^h, j = 1, 2, \dots, n_2^h, k = 1\}. \end{aligned}$$

200 The physical coordinates of the coarse grid points and fine grid points follow from the mappings $\mathbf{x}_i =$
201 $\mathbf{X}^c(\mathbf{r}_i)$ and $\mathbf{x}_i = \mathbf{X}^f(\mathbf{r}_i)$, respectively. We denote a grid function by

$$202 \quad \mathbf{u}_i = \mathbf{u}_{i,j,k} = \mathbf{u}(\mathbf{x}_i),$$

203 where \mathbf{u} can be either a scalar or vector. To distinguish between the continuous variables and the corre-
204 sponding approximations on the grid, we use \mathbf{c}_i and \mathbf{f}_i to denote the grid functions for the approximations
205 of $\mathbf{C}(\mathbf{x}_i)$ and $\mathbf{F}(\mathbf{x}_i)$, respectively. Let \mathbf{c} and \mathbf{f} be the vector representations of the grid functions \mathbf{c}_i and
206 \mathbf{f}_i respectively. The elements of \mathbf{c} and \mathbf{f} are ordered in the following way:

- 207 a). for each grid point \mathbf{x}_i , there is a 3×1 vector, say $\mathbf{c}_i = (c_i^{(1)}, c_i^{(2)}, c_i^{(3)})^T$ and $\mathbf{f}_i = (f_i^{(1)}, f_i^{(2)}, f_i^{(3)})^T$;
208 b). the grid points are ordered such that they first loop over $r^{(1)}$ direction (i), then $r^{(2)}$ direction (j),
209 and finally $r^{(3)}$ direction (k) as

$$210 \quad \mathbf{c} = [c_{1,1,1}^{(1)}, c_{1,1,1}^{(2)}, c_{1,1,1}^{(3)}, c_{2,1,1}^{(1)}, c_{2,1,1}^{(2)}, c_{2,1,1}^{(3)}, \dots]^T, \quad \mathbf{f} = [f_{1,1,1}^{(1)}, f_{1,1,1}^{(2)}, f_{1,1,1}^{(3)}, f_{2,1,1}^{(1)}, f_{2,1,1}^{(2)}, f_{2,1,1}^{(3)}, \dots]^T.$$

211 We note that \mathbf{c} contains the ghost point values for $k = n_3^{2h} + 1$, but \mathbf{f} does not contain any ghost point
212 values.

213 In the spatial discretization, we only use ghost points in the coarse domain and do not use ghost points
214 in the fine domain. Comparing with the traditional approach of using ghost points in both domains, the
215 system of linear equations at the interface becomes smaller and has a better structure. For the rest of the
216 paper, the \sim over an operator represents that the operator applies to a grid function with ghost points.
217 We approximate the elastic wave equation (2.2) in Ω^c by

$$218 \quad (3.7) \quad \left((\rho^{2h} \otimes \mathbf{I})(J^{2h} \otimes \mathbf{I}) \frac{d^2 \mathbf{c}}{dt^2} \right)_{\mathbf{i}} = \tilde{\mathcal{L}}_{\mathbf{i}}^{2h} \mathbf{c}, \quad \mathbf{i} \in I_{\Omega^c}, \quad t > 0,$$

219 where ρ^{2h} and J^{2h} are $n_1^{2h} n_2^{2h} n_3^{2h} \times n_1^{2h} n_2^{2h} n_3^{2h}$ diagonal matrices with the diagonal elements $\rho_{\mathbf{i}}^{2h} = \rho^c(\mathbf{x}_i)$
220 and $J_{\mathbf{i}}^{2h} = J^c(\mathbf{x}_i)$, $\mathbf{i} \in I_{\Omega^c}$; the matrix \mathbf{I} is a 3×3 identity matrix because the spatial dimension of the
221 governing equation is 3; finally, the discrete spatial operator is

$$222 \quad (3.8) \quad \tilde{\mathcal{L}}^{2h} \mathbf{c} = \left(\sum_{l=1}^2 Q_l^{2h}(N_{ll}^{2h}) \mathbf{c} + \tilde{G}_3^{2h}(N_{33}^{2h}) \mathbf{c} + \sum_{l=1}^3 \sum_{m=1, m \neq l}^3 D_l^{2h}(N_{lm}^{2h} D_m^{2h} \mathbf{c}) \right),$$

223 which uses ghost points when compute $\tilde{G}_3^{2h}(N_{33}^{2h}) \mathbf{c}$. In Appendix A, the terms $Q_l^{2h}(N_{ll}^{2h}) \mathbf{c}$, $\tilde{G}_3^{2h}(N_{33}^{2h}) \mathbf{c}$ and
224 $D_l^{2h}(N_{lm}^{2h} D_m^{2h} \mathbf{c})$ are presented, which approximate $\bar{\partial}_l(N_{ll} \bar{\partial}_l \mathbf{C})$, $\bar{\partial}_3(N_{33} \bar{\partial}_3 \mathbf{C})$ and $\bar{\partial}_l(N_{lm} \bar{\partial}_m \mathbf{C})$, respectively.
225

226 Next, we approximate the elastic wave equation (2.6) on the fine grid points. For all fine grid points
227 that are not located at the interface Γ , the semi-discretization is

$$227 \quad (3.9) \quad \left((\rho^h \otimes \mathbf{I})(J^h \otimes \mathbf{I}) \frac{d^2 \mathbf{f}}{dt^2} \right)_{\mathbf{i}} = \mathcal{L}_{\mathbf{i}}^h \mathbf{f}, \quad \mathbf{i} \in I_{\Omega^f} \setminus I_{\Gamma^f}, \quad t > 0.$$

228 Here, ρ^h and J^h are $n_1^h n_2^h n_3^h \times n_1^h n_2^h n_3^h$ diagonal matrices with the diagonal elements $\rho_{\mathbf{i}}^h = \rho^f(\mathbf{x}_i)$ and
229 $J_{\mathbf{i}}^h = J^f(\mathbf{x}_i)$, $\mathbf{i} \in I_{\Omega^f}$. And the discrete spatial operator is

$$230 \quad (3.10) \quad \mathcal{L}^h \mathbf{f} = \left(\sum_{l=1}^2 Q_l^h(N_{ll}^h) \mathbf{f} + G_3^h(N_{33}^h) \mathbf{f} + \sum_{l=1}^3 \sum_{m=1, m \neq l}^3 D_l^h(N_{lm}^h D_m^h \mathbf{f}) \right).$$

231 Here, the term $G_3^h(N_{33}^h) \mathbf{f}$ approximating $\bar{\partial}_3(N_{33} \bar{\partial}_3 \mathbf{F})$ without using any ghost points is presented in
232 Appendix A; the terms $Q_l^h(N_{ll}^h) \mathbf{f}$ and $D_l^h(N_{lm}^h D_m^h \mathbf{f})$ are defined similar as those in (3.8) and are used to
233 approximate $\bar{\partial}_l(N_{ll} \bar{\partial}_l \mathbf{F})$ and $\bar{\partial}_l(N_{lm} \bar{\partial}_m \mathbf{F})$, respectively.

234 For the approximation at the interface Γ , we obtain the numerical solution using a scaled interpolation
235 operator

$$236 \quad (3.11) \quad \mathbf{f}_{\mathbf{i}} = \mathcal{P}_{\mathbf{i}}(\mathbf{c}), \quad \mathbf{i} \in I_{\Gamma^f},$$

237 which imposes the continuity of the solution at the interface Γ . For energy stability, the operator \mathcal{P} must
238 be of a specific form

$$239 \quad (3.12) \quad \mathcal{P} = \left((J_{\Gamma}^h \Lambda^h)^{-\frac{1}{2}} \mathbf{P} (J_{\Gamma}^{2h} \Lambda^{2h})^{\frac{1}{2}} \right) \otimes \mathbf{I}.$$

240 Here, J_{Γ}^h and Λ^h are $n_1^h n_2^h \times n_1^h n_2^h$ diagonal matrices with diagonal elements $J_{\Gamma, \mathbf{i}}^h = J^f(\mathbf{x}_i)$ and $\Lambda_{\mathbf{i}}^h =$
241 $\Lambda^f(\mathbf{x}_i)$, $\mathbf{i} \in I_{\Gamma^f}$, with Λ^f is given in (2.8). Similarly, J_{Γ}^{2h} and Λ^{2h} are $n_1^{2h} n_2^{2h} \times n_1^{2h} n_2^{2h}$ diagonal matrices
242 with diagonal elements $J_{\Gamma, \mathbf{i}}^{2h} = J^c(\mathbf{x}_i)$ and $\Lambda_{\mathbf{i}}^{2h} = \Lambda^c(\mathbf{x}_i)$, $\mathbf{i} \in I_{\Gamma^c}$, with Λ^c is given in (2.8). Finally,
243 \mathbf{P} is an interpolation operator of size $n_1^h n_2^h \times n_1^{2h} n_2^{2h}$ for scalar grid functions at Γ^c . Since the spatial
244 discretization is fourth order accurate, we also use a fourth order interpolation. With mesh refinement
245 ratio 1 : 2, the stencils \mathbf{P} have four cases as illustrated in Figure 3. Consequently, the scaled interpolation
246 operator \mathcal{P} is also fourth order accurate.

247 In the implementation of our scheme, we use (3.11) to obtain the solution at the interface of the fine
 248 domain. However, in the energy analysis in Sec. 3.3, it is more convenient to use the equivalent form

$$249 \quad (3.13) \quad \left((\rho^h \otimes \mathbf{I})(J^h \otimes \mathbf{I}) \frac{d^2 \mathbf{f}}{dt^2} \right)_i = \mathcal{L}_i^h \mathbf{f} + \boldsymbol{\eta}_i, \quad i \in I_{\Gamma^f}$$

250 with

$$251 \quad (3.14) \quad \boldsymbol{\eta} = ((\rho^h J^h) \otimes \mathbf{I}) \mathcal{P} \left(((\rho^{2h} J^{2h}) \otimes \mathbf{I})^{-1} \tilde{\mathcal{L}}^{2h} \mathbf{c} \right) - \mathcal{L}^h \mathbf{f}.$$

252 The variable $\boldsymbol{\eta}$ in (3.14) is approximately zero with a second order truncation error, which is of the same
 253 order as the boundary stencil of the SBP operator. Hence, $\boldsymbol{\eta}$ does not affect the order of truncation
 254 error in the spatial discretization. For the simplicity of analysis, we introduce a general notation for the
 255 schemes (3.9) and (3.13) in the fine domain Ω^f ,

$$256 \quad (3.15) \quad \left((\rho^h \otimes \mathbf{I})(J^h \otimes \mathbf{I}) \frac{d^2 \mathbf{f}}{dt^2} \right)_i = \hat{\mathcal{L}}_i^h \mathbf{f} = \begin{cases} \mathcal{L}_i^h \mathbf{f} + \boldsymbol{\eta}_i, & i \in I_{\Gamma^f} \\ \mathcal{L}_i^h \mathbf{f}, & i \in I_{\Omega^f} \setminus I_{\Gamma^f} \end{cases} \quad t > 0.$$

258 The following condition imposes continuity of traction at the interface, the first equation in (2.7),

$$259 \quad (3.16) \quad \left(((\Lambda^{2h} J_\Gamma^{2h}) \otimes \mathbf{I})^{-1} \tilde{\mathcal{A}}_3^{2h} \mathbf{c} \right)_i = \mathcal{R}_i \left(((\Lambda^h J_\Gamma^h) \otimes \mathbf{I})^{-1} (\mathcal{A}_3^h \mathbf{f} - h_3 \omega_1 \boldsymbol{\eta}) \right), \quad i \in I_{\Gamma^c}.$$

260 Here, $((\Lambda^{2h} J_\Gamma^{2h}) \otimes \mathbf{I})^{-1} \tilde{\mathcal{A}}_3^{2h} \mathbf{c}$ and $((\Lambda^h J_\Gamma^h) \otimes \mathbf{I})^{-1} \mathcal{A}_3^h \mathbf{f}$ are approximations of the traction at the interface
 261 on the coarse grid and fine grid, respectively. The definitions of $\tilde{\mathcal{A}}_3^{2h} \mathbf{c}$ and $\mathcal{A}_3^h \mathbf{f}$ are given in Appendix A.
 262 The operator \mathcal{R} is a scaled restriction operator with the structure

$$263 \quad (3.17) \quad \mathcal{R} = \left((J_\Gamma^{2h} \Lambda^{2h})^{-\frac{1}{2}} \mathbf{R} (J_\Gamma^h \Lambda^h)^{\frac{1}{2}} \right) \otimes \mathbf{I},$$

264 where the stencils of \mathbf{R} in Figure 4 are determined by the compatibility condition $\mathbf{R} = \frac{1}{4} \mathbf{P}^T$. It is a
 265 restriction operator of size $n_1^{2h} n_2^{2h} \times n_1^h n_2^h$ for scalar grid functions at Γ^f . Finally, $h_3 \omega_1 \boldsymbol{\eta}$ in (3.16) is a term
 266 essential for stability, because in the stability analysis in the next section it cancels out $\boldsymbol{\eta}$ in the fine domain
 267 spatial discretization (3.15). The term is smaller than the truncation error of spatial discretization, so it
 268 does not affect the overall order of truncation error. Hence, (3.16) is a sufficiently accurate approximation
 269 for the continuity of traction at the interface. As will be seen later, the compatibility condition, as well
 270 as the scaling of the interpolation and restriction operators, are important for energy stability [11]. We
 271 also remark that the condition (3.16) determines the ghost points values in the coarse domain.

272 Let \mathbf{u} and \mathbf{v} be grid functions in the coarse domain Ω^c . We define the discrete inner product at the
 273 interface by

$$274 \quad (3.18) \quad \langle \mathbf{u}, \mathbf{v} \rangle_{2h} = 4h_1 h_2 \sum_{i=1}^{n_1^{2h}} \sum_{j=1}^{n_2^{2h}} J_{\Gamma, i, j, n_3^{2h}}^{2h} \Lambda_{i, j, n_3^{2h}}^{2h} (\mathbf{u}_{i, j, n_3^{2h}} \cdot \mathbf{v}_{i, j, n_3^{2h}}).$$

275 Similarly, the discrete inner product at the interface for fine domain Ω^f is defined as

$$276 \quad (3.19) \quad \langle \mathbf{u}, \mathbf{v} \rangle_h = h_1 h_2 \sum_{i=1}^{n_1^h} \sum_{j=1}^{n_2^h} J_{\Gamma, i, j, 1}^h \Lambda_{i, j, 1}^h (\mathbf{u}_{i, j, 1} \cdot \mathbf{v}_{i, j, 1})$$

277 when \mathbf{u} and \mathbf{v} are grid functions in fine domain Ω^f . Then we have the following lemma for the interpolation
 278 and restriction operators.

279 LEMMA 3.1. *Let \mathbf{c} and \mathbf{f} be grid functions at the interface for coarse domain and fine domain, re-
 280 spectively. Then the interpolation operator \mathcal{P} and the restriction operator \mathcal{R} satisfy*

$$281 \quad (3.20) \quad \langle \mathcal{P} \mathbf{c}, \mathbf{f} \rangle_h = \langle \mathbf{c}, \mathcal{R} \mathbf{f} \rangle_{2h}$$

282 if the compatibility condition $\mathbf{R} = \frac{1}{4} \mathbf{P}^T$ holds.

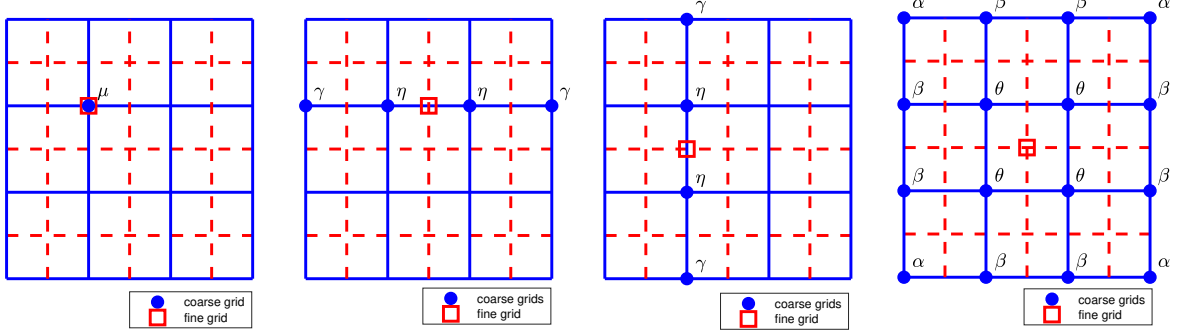


FIG. 3. The sketch for the stencils of fourth order interpolation operator \mathbf{P} in two dimensions with parameters $\gamma = -\frac{1}{16}$, $\eta = \frac{9}{16}$, $\mu = 1$, $\alpha = \frac{1}{256}$, $\beta = -\frac{9}{256}$ and $\theta = \frac{81}{256}$.

283 Proof. From (3.18)–(3.19), the definition of \mathcal{P} in (3.12) and \mathcal{R} in (3.17), we obtain

$$284 \quad \langle \mathcal{P}\mathbf{c}, \mathbf{f} \rangle_h = h_1 h_2 \left[\left((J_\Gamma^h \Lambda^h)^{\frac{1}{2}} \mathbf{P} (J_\Gamma^{2h} \Lambda^{2h})^{\frac{1}{2}} \otimes \mathbf{I} \right) \mathbf{c} \right]^T \mathbf{f}$$

$$285 \quad = 4h_1 h_2 \mathbf{c}^T \left[\left((J_\Gamma^{2h} \Lambda^{2h})^{\frac{1}{2}} \frac{1}{4} \mathbf{P}^T (J_\Gamma^h \Lambda^h)^{\frac{1}{2}} \otimes \mathbf{I} \right) \mathbf{f} \right]$$

$$286 \quad 287 \quad = 4h_1 h_2 \mathbf{c}^T \left[\left((J_\Gamma^{2h} \Lambda^{2h})^{\frac{1}{2}} \mathbf{R} (J_\Gamma^h \Lambda^h)^{\frac{1}{2}} \otimes \mathbf{I} \right) \mathbf{f} \right] = \langle \mathbf{c}, \mathcal{R}\mathbf{f} \rangle_{2h} \quad \square$$

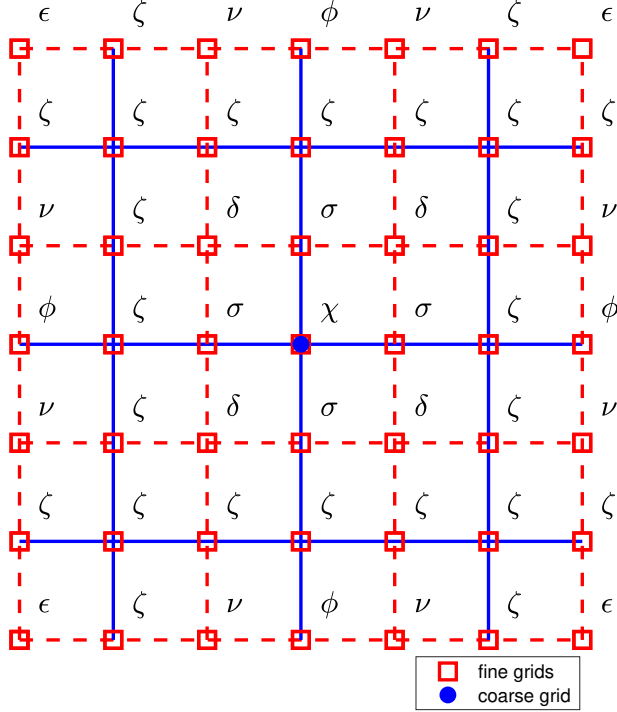


FIG. 4. The sketch for the stencil of fourth order restriction operator \mathbf{R} in two dimensions with parameters $\epsilon = \frac{1}{1024}$, $\nu = -\frac{9}{1024}$, $\phi = -\frac{16}{1024}$, $\delta = \frac{81}{1024}$, $\sigma = \frac{144}{1024}$, $\chi = \frac{256}{1024}$ and $\zeta = 0$.

288 3.3. Energy estimate. In this section, we derive an energy estimate for the semi-discretization
289 (3.7) and (3.15) in Sec. 3.2. Let \mathbf{u}, \mathbf{v} be grid functions in the coarse domain Ω^c and define the three

290 dimensional discrete scalar product in Ω^c as

$$291 \quad (3.21) \quad (\mathbf{v}, \mathbf{u})_{2h} = 8h_1 h_2 h_3 \sum_{i=1}^{n_1^{2h}} \sum_{j=1}^{n_2^{2h}} \sum_{k=1}^{n_3^{2h}} \omega_k J_{i,j,k}^{2h} (\mathbf{v}_{i,j,k} \cdot \mathbf{u}_{i,j,k}).$$

292 Similarly, define the three dimensional discrete scalar product in Ω^f as

$$293 \quad (3.22) \quad (\mathbf{v}, \mathbf{u})_h = h_1 h_2 h_3 \sum_{i=1}^{n_1^h} \sum_{j=1}^{n_2^h} \sum_{k=1}^{n_3^h} \omega_k J_{i,j,k}^h (\mathbf{v}_{i,j,k} \cdot \mathbf{u}_{i,j,k}),$$

294 where \mathbf{u} and \mathbf{v} are grid functions in the fine domain Ω^f . Now, we are ready to state the energy estimate
295 of the proposed schemes in Section 3.2.

296 THEOREM 3.2. *The semi-discretization (3.7) and (3.15) is energy stable if the interface conditions
297 (3.11) and (3.16) are satisfied.*

298 *Proof.* Forming the inner product between (3.7) and $8h_1 h_2 h_3 \omega_k \mathbf{c}_t$, and summing over i, j, k , we have

$$299 \quad (3.23) \quad (\mathbf{c}_t, (\rho^{2h} \otimes \mathbf{I}) \mathbf{c}_{tt})_{2h} = (\mathbf{c}_t, (J^{2h} \otimes \mathbf{I})^{-1} \tilde{\mathcal{L}}^{2h} \mathbf{c})_{2h} = -\mathcal{S}_{2h}(\mathbf{c}_t, \mathbf{c}) + B_{2h}(\mathbf{c}_t, \mathbf{c}),$$

300 where $\mathcal{S}_{2h}(\mathbf{c}_t, \mathbf{c})$ is a symmetric and positive definite bilinear form given in Appendix B, the boundary
301 term $B_{2h}(\mathbf{c}_t, \mathbf{c})$ is given by

$$302 \quad (3.24) \quad B_{2h}(\mathbf{c}_t, \mathbf{c}) = 4h_1 h_2 \sum_{\mathbf{i} \in I_{\Gamma^c}} \frac{d\mathbf{c}_i}{dt} \cdot (\tilde{A}_3^{2h} \mathbf{c})_{\mathbf{i}}.$$

303 Forming the inner product between (3.15) and $h_1 h_2 h_3 \omega_k \mathbf{f}_t$, and summing over i, j, k , we obtain

$$304 \quad (3.25) \quad (\mathbf{f}_t, (\rho^h \otimes \mathbf{I}) \mathbf{f}_{tt})_h = (\mathbf{f}_t, (J^h \otimes \mathbf{I})^{-1} \hat{\mathcal{L}}^h \mathbf{f})_h = -\mathcal{S}_h(\mathbf{f}_t, \mathbf{f}) + B_h(\mathbf{f}_t, \mathbf{f}) + h_1 h_2 h_3 \omega_1 \sum_{\mathbf{i} \in I_{\Gamma^f}} \frac{d\mathbf{f}_i}{dt} \cdot \boldsymbol{\eta}_{\mathbf{i}}.$$

305 Here, \mathcal{S}_h is also a symmetric and positive definite bilinear form given in Appendix B. The boundary term
306 $B_h(\mathbf{f}_t, \mathbf{f})$ has the following form

$$307 \quad (3.26) \quad B_h(\mathbf{f}_t, \mathbf{f}) = -h_1 h_2 \sum_{\mathbf{i} \in I_{\Gamma^f}} \frac{d\mathbf{f}_i}{dt} \cdot (A_3^h \mathbf{f})_{\mathbf{i}}.$$

308 Adding (3.23) and (3.25) together, we have

$$310 \quad (3.27) \quad \frac{d}{dt} [(\mathbf{f}_t, (\rho^h \otimes \mathbf{I}) \mathbf{f}_t)_h + \mathcal{S}_h(\mathbf{f}, \mathbf{f}) + (\mathbf{c}_t, (\rho^{2h} \otimes \mathbf{I}) \mathbf{c}_t)_{2h} + \mathcal{S}_{2h}(\mathbf{c}, \mathbf{c})] = \\ 311 \quad 2B_h(\mathbf{f}_t, \mathbf{f}) + 2B_{2h}(\mathbf{c}_t, \mathbf{c}) + 2h_1 h_2 h_3 \omega_1 \sum_{\mathbf{i} \in I_{\Gamma^f}} \frac{d\mathbf{f}_i}{dt} \cdot \boldsymbol{\eta}_{\mathbf{i}}.$$

313 Substituting (3.26) and (3.24) into (3.27) and combining the definitions of the scalar product at the
314 interface (3.18)–(3.19), the continuity of solution at the interface (3.11) and Lemma 3.1, we get

$$315 \quad \frac{d}{dt} [(\mathbf{f}_t, (\rho^h \otimes \mathbf{I}) \mathbf{f}_t)_h + \mathcal{S}_h(\mathbf{f}, \mathbf{f}) + (\mathbf{c}_t, (\rho^{2h} \otimes \mathbf{I}) \mathbf{c}_t)_{2h} + \mathcal{S}_{2h}(\mathbf{c}, \mathbf{c})] \\ 316 \quad = 2 \langle \mathbf{f}_t, ((\Lambda^h J_{\Gamma}^h) \otimes \mathbf{I})^{-1} (-\mathcal{A}_3^h \mathbf{f} + h_3 \omega_1 \boldsymbol{\eta}) \rangle_h + 2 \langle \mathbf{c}_t, ((\Lambda^{2h} J_{\Gamma}^{2h}) \otimes \mathbf{I})^{-1} \tilde{\mathcal{A}}_3^{2h} \mathbf{c} \rangle_{2h} \\ 317 \quad = 2 \langle \mathcal{P} \mathbf{c}_t, ((\Lambda^h J_{\Gamma}^h) \otimes \mathbf{I})^{-1} (-\mathcal{A}_3^h \mathbf{f} + h_3 \omega_1 \boldsymbol{\eta}) \rangle_h + 2 \langle \mathbf{c}_t, ((\Lambda^{2h} J_{\Gamma}^{2h}) \otimes \mathbf{I})^{-1} \tilde{\mathcal{A}}_3^{2h} \mathbf{c} \rangle_{2h} \\ 318 \quad = 2 \langle \mathbf{c}_t, \mathcal{R}((\Lambda^h J_{\Gamma}^h) \otimes \mathbf{I})^{-1} (-\mathcal{A}_3^h \mathbf{f} + h_3 \omega_1 \boldsymbol{\eta}) \rangle_{2h} + 2 \langle \mathbf{c}_t, ((\Lambda^{2h} J_{\Gamma}^{2h}) \otimes \mathbf{I})^{-1} \tilde{\mathcal{A}}_3^{2h} \mathbf{c} \rangle_{2h} = 0.$$

320 Note that the discrete energy for the semi-discretization (3.7) and (3.15) is given by $(\mathbf{f}_t, (\rho^h \otimes \mathbf{I}) \mathbf{f}_t)_h +$
321 $\mathcal{S}_h(\mathbf{f}, \mathbf{f}) + (\mathbf{c}_t, (\rho^{2h} \otimes \mathbf{I}) \mathbf{c}_t)_{2h} + \mathcal{S}_{2h}(\mathbf{c}, \mathbf{c})$. \square

322 **4. The temporal discretization.** The equations are advanced in time with an explicit fourth
 323 order accurate predictor-corrector time integration method. Like all explicit time stepping methods, the
 324 time step must not exceed the CFL stability limit. By a similar analysis as in [16], we require

$$325 \quad \Delta_t \leq C_{\text{cfl}} \min\{h_1, h_2, h_3\} / \sqrt{\kappa_{\max}},$$

326 where κ_{\max} is the maximum eigenvalue of the matrices

$$327 \quad T_i^{\{f,c\}} = \frac{1}{\rho^{\{f,c\}}(\mathbf{r}_i)} \begin{pmatrix} Tr(N_{11}^{\{f,c\}}(\mathbf{r}_i)) & Tr(N_{12}^{\{f,c\}}(\mathbf{r}_i)) & Tr(N_{13}^{\{f,c\}}(\mathbf{r}_i)) \\ Tr(N_{21}^{\{f,c\}}(\mathbf{r}_i)) & Tr(N_{22}^{\{f,c\}}(\mathbf{r}_i)) & Tr(N_{23}^{\{f,c\}}(\mathbf{r}_i)) \\ Tr(N_{31}^{\{f,c\}}(\mathbf{r}_i)) & Tr(N_{32}^{\{f,c\}}(\mathbf{r}_i)) & Tr(N_{33}^{\{f,c\}}(\mathbf{r}_i)) \end{pmatrix},$$

328 and $Tr(N_{lm}^{\{f,c\}}(\mathbf{r}_i))$ represents the trace of 3×3 matrix $N_{lm}^{\{f,c\}}(\mathbf{r}_i)$. Note that κ_{\max} is related to the
 329 material properties $\mu^{\{f,c\}}, \lambda^{\{f,c\}}$ and $\rho^{\{f,c\}}$. The notation $\{\cdot, \cdot\}$ represents the component-wise identities.
 330 We choose the Courant number $C_{\text{cfl}} = 1.3$, which has been shown to work well in practical problems
 331 [14, 16]. The Courant number shall not be chosen too close to the stability limit so that noticeable
 332 reflections at mesh refinement interfaces can be avoided [3]. In the following, we give detailed procedures
 333 about how we apply the fourth order time integrator to the semidiscretizations (3.7) and (3.15).

334 Let \mathbf{c}^n and \mathbf{f}^n denote the numerical approximations of $\mathbf{C}(\mathbf{x}, t_n), \mathbf{x} \in \Omega^c$ and $\mathbf{F}(\mathbf{x}, t_n), \mathbf{x} \in \Omega^f$, respectively.
 335 Here, $t_n = n\Delta_t, n = 0, 1, \dots$ and $\Delta_t > 0$ is a constant time step. We present the fourth order
 336 time integrator with predictor and corrector in Algorithm 4.1.

337 **Algorithm 4.1** Fourth order accurate time stepping for the semidiscretizations (3.7) and (3.15).

339 Given $\tilde{\mathbf{c}}^n, \tilde{\mathbf{c}}^{n-1}$ and $\mathbf{f}^n, \mathbf{f}^{n-1}$ that satisfy the discretized interface conditions.

- 340 • Compute the predictor at the interior grid points

$$341 \quad \mathbf{c}_i^{*,n+1} = 2\mathbf{c}_i^n - \mathbf{c}_i^{n-1} + \Delta_t^2 ((\rho^{2h} \otimes \mathbf{I})(J^{2h} \otimes \mathbf{I}))^{-1} \tilde{\mathcal{L}}_i^{2h} \mathbf{c}^n, \quad \mathbf{i} \in I_{\Omega^c},$$

$$343 \quad \mathbf{f}_i^{*,n+1} = 2\mathbf{f}_i^n - \mathbf{f}_i^{n-1} + \Delta_t^2 ((\rho^h \otimes \mathbf{I})(J^h \otimes \mathbf{I}))^{-1} \hat{\mathcal{L}}_i^h \mathbf{f}^n, \quad \mathbf{i} \in I_{\Omega^f} \setminus I_{\Gamma^f}.$$

- 344 • At the interface Γ , the values $\mathbf{f}_i^{*,n+1}$ are computed by the continuity of solution

$$345 \quad \mathbf{f}_i^{*,n+1} = \mathcal{P}_i(\mathbf{c}^{*,n+1}), \quad \mathbf{i} \in I_{\Gamma^f}.$$

- 346 • At the interface Γ , the ghost point values in $\tilde{\mathbf{c}}^{*,n+1}$ are computed by solving the equation for the
 347 continuity of traction

$$348 \quad (4.1) \quad \left(((\Lambda^{2h} J_\Gamma^{2h}) \otimes \mathbf{I})^{-1} \tilde{\mathcal{A}}_3^{2h} \mathbf{c}^{*,n+1} \right)_i = \mathcal{R}_i \left(((\Lambda^h J_\Gamma^h) \otimes \mathbf{I})^{-1} (\mathcal{A}_3^h \mathbf{f}^{*,n+1} - h_3 \omega_1 \boldsymbol{\eta}^{*,n+1}) \right), \mathbf{i} \in I_{\Gamma^c}.$$

- 349 • Evaluate the acceleration at all grid points

$$350 \quad \tilde{\mathbf{a}}_c^n = \frac{\tilde{\mathbf{c}}^{*,n+1} - 2\tilde{\mathbf{c}}^n + \tilde{\mathbf{c}}^{n-1}}{\Delta_t^2}, \quad \mathbf{a}_f^n = \frac{\mathbf{f}^{*,n+1} - 2\mathbf{f}^n + \mathbf{f}^{n-1}}{\Delta_t^2}.$$

- 351 • Compute the corrector at the interior grid points

$$352 \quad \mathbf{c}_i^{n+1} = \mathbf{c}_i^{*,n+1} + \frac{\Delta_t^4}{12} ((\rho^{2h} \otimes \mathbf{I})(J^{2h} \otimes \mathbf{I}))^{-1} \tilde{\mathcal{L}}_i^{2h} \mathbf{a}_c^n, \quad \mathbf{i} \in I_{\Omega^c},$$

$$354 \quad \mathbf{f}_i^{n+1} = \mathbf{f}_i^{*,n+1} + \frac{\Delta_t^4}{12} ((\rho^h \otimes \mathbf{I})(J^h \otimes \mathbf{I}))^{-1} \hat{\mathcal{L}}_i^h \mathbf{a}_f^n, \quad \mathbf{i} \in I_\Omega^f.$$

- 355 • At the interface Γ , the values \mathbf{f}_i^{n+1} are computed by the continuity of solution

$$356 \quad \mathbf{f}_i^{n+1} = \mathcal{P}_i(\mathbf{c}^{n+1}), \quad \mathbf{i} \in I_{\Gamma^f}.$$

- 357 • At the interface Γ , the ghost point values in $\tilde{\mathbf{c}}^{n+1}$ are computed by solving the equation for the
 358 continuity of traction

359 (4.2)
$$\left(\left((\Lambda^{2h} J_{\Gamma}^{2h}) \otimes \mathbf{I} \right)^{-1} \tilde{\mathcal{A}}_3^{2h} \mathbf{c}^{n+1} \right)_{\mathbf{i}} = \mathcal{R}_{\mathbf{i}} \left(\left((\Lambda^h J_{\Gamma}^h) \otimes \mathbf{I} \right)^{-1} (\mathcal{A}_3^h \mathbf{f}^{n+1} - h_3 \omega_1 \boldsymbol{\eta}^{n+1}) \right), \quad \mathbf{i} \in I_{\Gamma^c}.$$

360
 361
 362 In the Algorithm 4.1, we need to solve the linear systems for the continuity of traction at the interface
 363 Γ in both predictor step (4.1) and corrector step (4.2). The linear system matrices of (4.1) and (4.2) are
 364 the same. Therefore, we only present how to solve (4.1) in the predictor step.

365 There are $3n_1^{2h}n_2^{2h}$ unknowns and $3n_1^{2h}n_2^{2h}$ linear equations in (4.1). For large problems in three
 366 dimensions, it is very memory inefficient to calculate the LU-factorization. Therefore, we use iterative
 367 methods to solve the linear system in (4.1). In particular, we consider three different iterative methods:
 368 the block Jacobi iterative method, the conjugate gradient (CG) iterative method and the preconditioned
 369 conjugate gradient iterative method. The detailed methods and a comparison are given in Section 5.2.

370 **5. Numerical Experiments.** We present four numerical experiments. In Sec. 5.1, we verify the
 371 order of the convergence of the proposed scheme (3.7, 3.15, 3.11, 3.16). In Sec. 5.2, we present three
 372 iterative methods for solving the linear systems (4.1) and (4.2). The efficiency of the iterative methods
 373 is investigated and a comparison with the LU-factorization method is conducted. Next, in Sec. 5.3 we
 374 show that our schemes generate little reflection at the mesh refinement interface. Finally, the energy
 375 conservation property is verified in Sec. 5.4 with heterogeneous and discontinuous material properties.

376 **5.1. Verification of convergence rate.** We use the method of the manufactured solution to verify
 377 the fourth order convergence rate of the proposed scheme. We choose the mapping of the coarse domain
 378 Ω^c as

379
$$\mathbf{x} = \mathbf{X}^c(\mathbf{r}) = \begin{pmatrix} 2\pi r^{(1)} \\ 2\pi r^{(2)} \\ r^{(3)}\theta_i(r^{(1)}, r^{(2)}) + (1 - r^{(3)})\theta_b(r^{(1)}, r^{(2)}) \end{pmatrix},$$

380 where $0 \leq r^{(1)}, r^{(2)}, r^{(3)} \leq 1$, θ_i represents the interface surface geometry,

381 (5.1)
$$\theta_i(r^{(1)}, r^{(2)}) = \pi + 0.2 \sin(4\pi r^{(1)}) + 0.2 \cos(4\pi r^{(2)}),$$

382 and θ_b is the bottom surface geometry,

383
$$\theta_b(r^{(1)}, r^{(2)}) = 0.2 \exp\left(-\frac{(r^{(1)} - 0.6)^2}{0.04}\right) + 0.2 \exp\left(-\frac{(r^{(2)} - 0.6)^2}{0.04}\right).$$

384 As for the fine domain Ω^f , the mapping is chosen to be

385
$$\mathbf{x} = \mathbf{X}^f(\mathbf{r}) = \begin{pmatrix} 2\pi r^{(1)} \\ 2\pi r^{(2)} \\ r^{(3)}\theta_t(r^{(1)}, r^{(2)}) + (1 - r^{(3)})\theta_i(r^{(1)}, r^{(2)}) \end{pmatrix},$$

386 where $0 \leq r^{(1)}, r^{(2)}, r^{(3)} \leq 1$ and θ_t is the top surface geometry,

387
$$\theta_t(r^{(1)}, r^{(2)}) = 2\pi + 0.2 \exp\left(-\frac{(r^{(1)} - 0.5)^2}{0.04}\right) + 0.2 \exp\left(-\frac{(r^{(2)} - 0.5)^2}{0.04}\right).$$

388 In the entire domain, we choose the density

389
$$\rho(x^{(1)}, x^{(2)}, x^{(3)}) = 2 + \sin(x^{(1)} + 0.3) \sin(x^{(2)} + 0.3) \sin(x^{(3)} - 0.2),$$

390 and material parameters μ, λ

391
$$\mu(x^{(1)}, x^{(2)}, x^{(3)}) = 3 + \sin(3x^{(1)} + 0.1) \sin(3x^{(2)} + 0.1) \sin(x^{(3)}),$$

392 and

$$393 \quad \lambda(x^{(1)}, x^{(2)}, x^{(3)}) = 21 + \cos(x^{(1)} + 0.1) \cos(x^{(2)} + 0.1) \sin^2(3x^{(3)}).$$

394 In addition, we impose a boundary forcing on the top surface and Dirichlet boundary conditions for
 395 the other boundaries. The external forcing, top boundary forcing \mathbf{g} and initial conditions are chosen
 396 such that the solutions for both fine domain (\mathbf{F}) and coarse domain (\mathbf{C}) are $\mathbf{F}(\cdot, t) = \mathbf{C}(\cdot, t) = \mathbf{u}(\cdot, t) =$
 397 $(u_1(\cdot, t), u_2(\cdot, t), u_3(\cdot, t))^T$ with

$$398 \quad u_1(\cdot, t) = \cos(x^{(1)} + 0.3) \sin(x^{(2)} + 0.3) \sin(x^{(3)} + 0.2) \cos(t^2), \\ 399 \quad u_2(\cdot, t) = \sin(x^{(1)} + 0.3) \cos(x^{(2)} + 0.3) \sin(x^{(3)} + 0.2) \cos(t^2), \\ 400 \quad u_3(\cdot, t) = \sin(x^{(1)} + 0.2) \sin(x^{(2)} + 0.2) \cos(x^{(3)} + 0.2) \sin(t).$$

402 For example, for the boundary forcing at the top surface, we have

$$403 \quad \mathbf{g} = (g_1, g_2, g_3)^T = \sum_{i=1}^3 \left(\sum_{j=1}^3 M_{ij}^f \frac{\partial \mathbf{u}}{\partial x^{(j)}} \right) n_3^{f,+i},$$

404 where, M_{ij}^f and $n_3^{f,+i}$ are defined in (2.4) and (2.5), respectively.

405 The problem is evolved until final time $T = 0.5$. In Table 1, we use L_2 to represent the L^2 error in
 406 the entire domain $\Omega = \Omega^c \cup \Omega^f$. The notations L_2^f and L_2^c represent the L^2 error in the fine domain Ω^f
 407 and coarse domain Ω^c , respectively. The convergence rates are shown in the parentheses in Table 1. We
 408 observe that the convergence rate is fourth order for all cases. Even though the boundary accuracy of
 409 the SBP operator is only second order, the optimal convergence rate is fourth order. For a more detailed
 410 analysis of the convergence rate, we refer to [19, 20]. To solve the linear system for ghost point values,
 411 we use a block Jacobi iterative method. In the following section, we study two more iterative methods
 412 and compare them in terms of the condition number and the number of iterations.

$2h_1 = 2h_2 = 2h_3 = 2h$	L_2	L_2^f	L_2^c
$2\pi/24$	2.2227e-03	8.0442e-04	2.0720e-03
$2\pi/48$	1.4142e-04 (3.97)	5.1478e-05 (3.97)	1.3171e-04 (3.98)
$2\pi/96$	8.6166e-06 (4.04)	3.0380e-06 (4.08)	8.0632e-06 (4.03)

TABLE 1
The L^2 error and corresponding convergence rates of the fourth order SBP method

413 **5.2. Iterative methods.** In this section, we use the same example as in Sec. 5.1. For the proposed
 414 scheme (3.7, 3.15, 3.11, 3.16), we need to solve linear systems with $3n_1^{2h}n_2^{2h}$ unknown ghost point values on
 415 the coarse grid. At each time step, two linear systems with the same matrix are solved for the continuity
 416 of traction at the interface Γ .

417 We investigate three iterative methods: the block Jacobi method, the conjugate gradient method and
 418 the preconditioned conjugate gradient method. We note that the coefficient matrix of the linear system
 419 arising from the continuity of traction at interface Γ is not symmetric for this test problem. However, our
 420 experiment shows that both the conjugate gradient method and the preconditioned conjugate gradient
 421 method converge.

422 For the problem proposed in Sec. 5.1, the structure of the coefficient matrix of the linear system
 423 arising in (3.16) is shown in Figure 5, which is determined by the interpolation operator \mathcal{P} and restriction
 424 operator \mathcal{R} . In this example, we use $n_1^{2h} = n_2^{2h} = 13, n_3^{2h} = 7$. We choose the entries indicated by red color
 425 in Figure 5 to be the block Jacobi matrix in the block Jacobi iterative method and the preconditioning
 426 matrix in the preconditioned conjugate gradient method. The absolute error tolerance is set to be 10^{-7}
 427 for all three iterative methods and $h_1 = h_2 = h_3 = h$.

428 Table 2 shows the condition number of the original coefficient matrix, the block Jacobi matrix and
 429 the coefficient matrix after applying the preconditioning matrix. We observe that the condition number

$2h$	CG	Block Jacobi	Preconditioned CG
$2\pi/24$	37.78	24.96	4.01
$2\pi/48$	38.61	25.38	2.87
$2\pi/96$	39.14	25.43	2.25

TABLE 2

The condition number of the matrices in the conjugate gradient method, the block Jacobi method and the preconditioned conjugate gradient method

for preconditioned conjugate gradient method is smallest and is consistent with the results of iteration number for different iterative methods: there are around 44 iterations for the conjugate gradient method, 13 iterations for the block Jacobi method and 9 iterations for the preconditioned conjugate gradient method.

In comparison, we have also performed an LU factorization for the linear system when the mesh size $2h = 2\pi/96$, and the computation takes 40.6 GB memory. In contrast, with the block Jacobi method, the peak memory usage is only 1.2 GB. For large-scale problems, the memory usage becomes infeasible for the LU factorization.

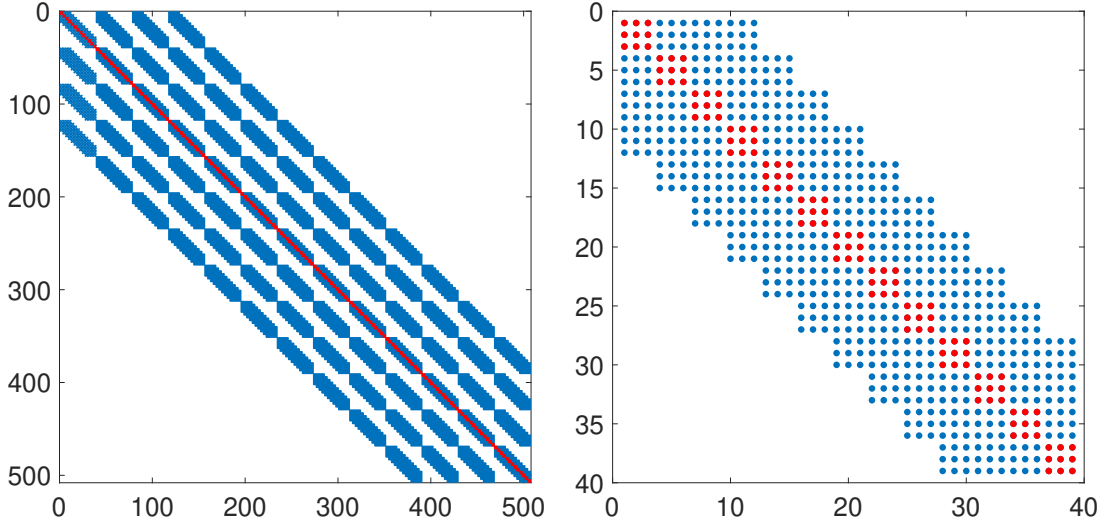


FIG. 5. The left panel is the structure of the coefficient matrix of the linear system (3.16). The right panel shows a close-up of one diagonal block.

5.3. Gaussian source. In this section, we perform a numerical simulation with a Gaussian source at the top surface and verify that the curved mesh refinement interface does not generate any artifacts.

We choose a flat top and bottom surface geometry

$$\theta_t(r^{(1)}, r^{(2)}) = 1000, \quad \theta_b(r^{(1)}, r^{(2)}) = 0,$$

respectively. The mesh refinement interface is parameterized by

$$\theta_i(r^{(1)}, r^{(2)}) = 800 + 20 \sin(4\pi r^{(1)}) + 20 \cos(4\pi r^{(2)}), \quad (5.2)$$

where $0 \leq r^{(1)}, r^{(2)}, r^{(3)} \leq 1$. In addition, the mapping in the coarse domain Ω^c and fine domain Ω^f are given by

$$\mathbf{x} = \mathbf{X}^c(\mathbf{r}) = \begin{pmatrix} 2000r^{(1)} \\ 2000r^{(2)} \\ r^{(3)}\theta_i(r^{(1)}, r^{(2)}) + (1 - r^{(3)})\theta_b(r^{(1)}, r^{(2)}) \end{pmatrix}$$

447 and

$$448 \quad \mathbf{x} = \mathbf{X}^f(\mathbf{r}) = \begin{pmatrix} 2000r^{(1)} \\ 2000r^{(2)} \\ r^{(3)}\theta_t(r^{(1)}, r^{(2)}) + (1 - r^{(3)})\theta_i(r^{(1)}, r^{(2)}) \end{pmatrix},$$

449 respectively. In the entire domain, we use the homogeneous material properties

$$450 \quad \rho(x^{(1)}, x^{(2)}, x^{(3)}) = 1.5 \times 10^3, \quad \mu(x^{(1)}, x^{(2)}, x^{(3)}) = 1.5 \times 10^9, \quad \lambda(x^{(1)}, x^{(2)}, x^{(3)}) = 3 \times 10^9.$$

451 At the top surface, the Gaussian source $\mathbf{g} = (g_1, g_2, g_3)^T$ is imposed as the Dirichlet data with
452 $g_1 = g_2 = 0$ and

$$453 \quad g_3 = 10^9 \exp\left(-\left(\frac{t - 4/44.2}{1/44.2}\right)^2\right) \exp\left(-\left(\frac{x^{(1)} - 1000}{12.5}\right)^2 - \left(\frac{x^{(2)} - 1000}{12.5}\right)^2\right).$$

454 Homogeneous Dirichlet boundary conditions are imposed at other boundaries. Both the initial conditions
455 and the external forcing are set to zero everywhere. For these material properties, the shear wave velocity
456 is $c_s = \sqrt{\mu/\rho} = 1000$. With the dominant wave frequency $f_0 = 44.2\sqrt{2}/(2\pi) \approx 10$, the corresponding
457 wavelength c_s/f_0 is approximately 100.

458 In the numerical schemes, we consider three different meshes: Mesh 1 is the Cartesian mesh without
459 any interface and $n_1 = n_2 = 201, n_3 = 101$ with n_i denotes the number of grid points in the direction $x^{(i)}$.
460 This corresponds to 10 grid points per wavelength and is considered as the reference solution. Mesh 2 is the
461 curvilinear mesh with a curved mesh refinement interface defined in (5.2) and $n_1^{2h} = n_2^{2h} = 101, n_3^{2h} = 41$,
462 $n_1^h = n_2^h = 201, n_3^h = 21$. The mesh size in Ω^f is approximately the same as the mesh size in the Cartesian
463 mesh. As a result, the waves are resolved with 5 grid points per wavelength in Ω^c . Mesh 3 is obtained
464 by refining Mesh 2 in all three spatial directions.

465 In Figure 6, we plot the component u_1 at $t = 0.2$ and $t = 0.4$. Some artifacts are observed in the
466 solution computed with the second mesh, which is due to the small number of grid points per wavelength
467 in Ω^c . The results become better when the finer curvilinear mesh is used. From Figure 7, we observe
468 that there is no obvious reflection at the mesh refinement interface for the component u_3 , and we have a
469 better result when a finer curvilinear mesh is used. The component u_2 is zero up to round-off error for
470 both the Cartesian mesh and curvilinear meshes and is not presented here.

471 **5.4. Energy conservation test.** To verify the energy conservation property of the scheme, we
472 perform computation without external source term, but with a Gaussian initial data centered at the
473 origin of the computational domain. The computational domain is chosen to be the same as in Sec. 5.1.
474 The material property is heterogeneous and discontinuous: for the fine domain Ω^f , the density varies
475 according to

$$476 \quad \rho^f(x^{(1)}, x^{(2)}, x^{(3)}) = 3 + \sin(2x^{(1)} + 0.3) \cos(x^{(2)} + 0.3) \sin(2x^{(3)} - 0.2),$$

477 and material parameters satisfy

$$478 \quad \mu^f(x^{(1)}, x^{(2)}, x^{(3)}) = 2 + \cos(3x^{(1)} + 0.1) \sin(3x^{(2)} + 0.1) \sin(x^{(3)})^2,$$

$$479 \quad \lambda^f(x^{(1)}, x^{(2)}, x^{(3)}) = 15 + \cos(x^{(1)} + 0.1) \sin(4x^{(2)} + 0.1) \sin(3x^{(3)})^2;$$

481 for the coarse domain Ω^c , the density varies according to

$$482 \quad \rho^c(x^{(1)}, x^{(2)}, x^{(3)}) = 2 + \sin(x^{(1)} + 0.3) \sin(x^{(2)} + 0.3) \sin(2x^{(3)} - 0.2),$$

483 and material parameters satisfy

$$484 \quad \mu^c(x^{(1)}, x^{(2)}, x^{(3)}) = 3 + \sin(3x^{(1)} + 0.1) \sin(3x^{(2)} + 0.1) \sin(x^{(3)}),$$

$$485 \quad \lambda^c(x^{(1)}, x^{(2)}, x^{(3)}) = 21 + \cos(x^{(1)} + 0.1) \cos(x^{(2)} + 0.1) \sin(3x^{(3)})^2.$$

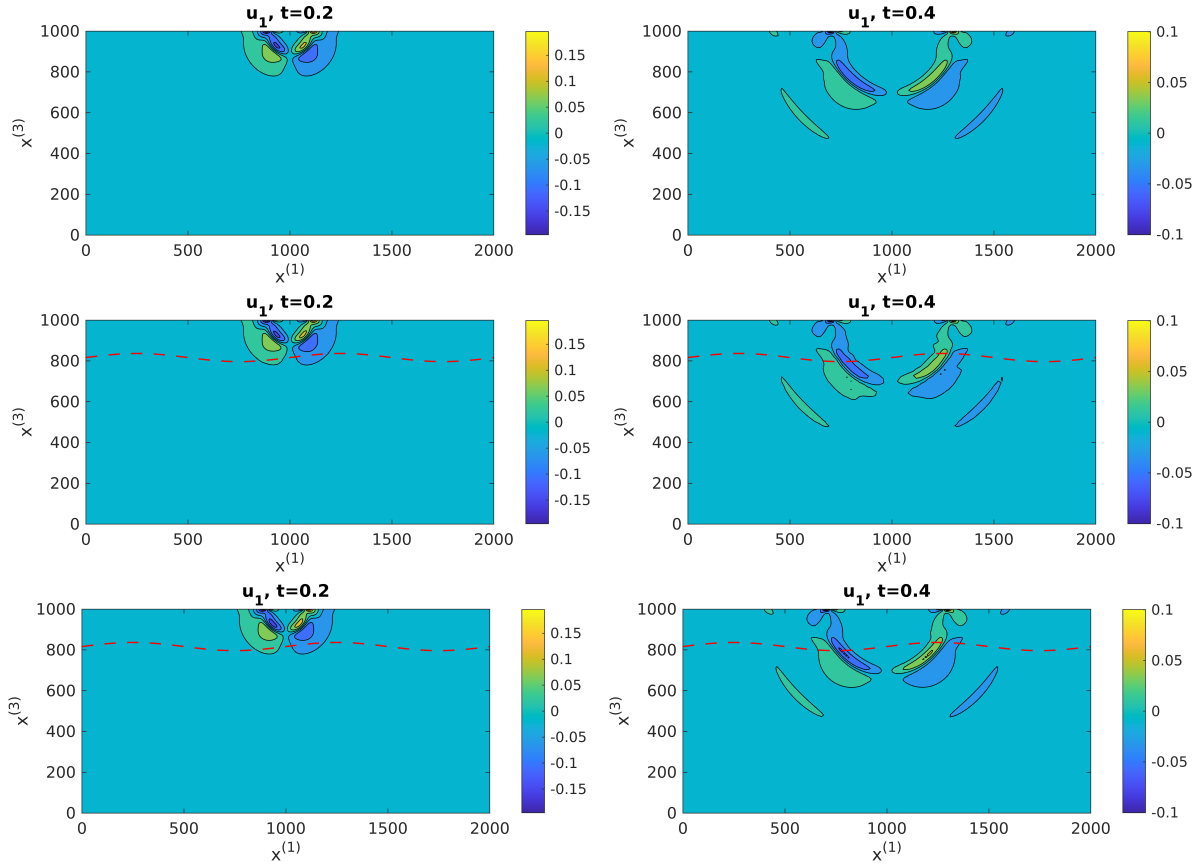


FIG. 6. The graphs for u_1 . In the top, middle and bottom panel, we show numerical solutions at $t = 0.2$ and $t = 0.4$ computed with Mesh 1 (uniform Cartesian grid without any interface), Mesh 2 (curved interface) and Mesh 3 (a refinement of Mesh 2), respectively. The curved interfaces are marked with the red dash lines.

487 The initial Gaussian data is given by $\mathbf{C}(\cdot, 0) = \mathbf{F}(\cdot, 0) = \mathbf{u}(\cdot, 0) = (u_1(\cdot, 0), u_2(\cdot, 0), u_3(\cdot, 0))^T$ with

488
$$u_1(\cdot, 0) = \exp\left(-\frac{(x^{(1)} - \pi)^2}{0.1}\right) \exp\left(-\frac{(x^{(2)} - \pi)^2}{0.1}\right) \exp\left(-\frac{(x^{(3)} - \pi)^2}{0.1}\right),$$

489
$$u_2(\cdot, 0) = \exp\left(-\frac{(x^{(1)} - \pi)^2}{0.2}\right) \exp\left(-\frac{(x^{(2)} - \pi)^2}{0.2}\right) \exp\left(-\frac{(x^{(3)} - \pi)^2}{0.2}\right),$$

490
$$u_3(\cdot, 0) = \exp\left(-\frac{(x^{(1)} - \pi)^2}{0.1}\right) \exp\left(-\frac{(x^{(2)} - \pi)^2}{0.2}\right) \exp\left(-\frac{(x^{(3)} - \pi)^2}{0.2}\right).$$

492 The grid spacing in the parameter space for the coarse domain Ω^c is $2h_1 = 2h_2 = 2h_3 = \frac{\pi}{24}$ and for the
493 fine domain Ω^f is $h_1 = h_2 = h_3 = \frac{\pi}{48}$, that is we have $25 \times 25 \times 13$ grid points in the coarse domain Ω^c
494 and $49 \times 49 \times 25$ grid points in the fine domain Ω^f .

495 The semi-discrete energy is given by $(\mathbf{f}_t, (\rho^h \otimes \mathbf{I})\mathbf{f}_t)_h + \mathcal{S}_h(\mathbf{f}, \mathbf{f}) + (\mathbf{c}_t, (\rho^{2h} \otimes \mathbf{I})\mathbf{c}_t)_{2h} + \mathcal{S}_{2h}(\mathbf{c}, \mathbf{c})$, see
496 (3.27). By using the same approach as for the isotropic elastic wave equation, see [14, 16], the expression
497 for the fully discrete energy reads

498
$$E^{n+1/2} = \left\| (\rho^h \otimes \mathbf{I})^{\frac{1}{2}} \frac{\mathbf{f}^{n+1} - \mathbf{f}^n}{\Delta t} \right\|_h^2 + S_h(\mathbf{f}^{n+1}, \mathbf{f}^n) - \frac{(\Delta t)^2}{12} \left((J^h \otimes \mathbf{I})^{-1} \mathcal{L}^h \mathbf{f}^{n+1}, (\rho^h \otimes \mathbf{I})^{-1} (J^h \otimes \mathbf{I})^{-1} \mathcal{L}^h \mathbf{f}^n \right)_h$$

499
$$+ \left\| (\rho^{2h} \otimes \mathbf{I})^{\frac{1}{2}} \frac{\mathbf{c}^{n+1} - \mathbf{c}^n}{\Delta t} \right\|_{2h}^2 + S_{2h}(\mathbf{c}^{n+1}, \mathbf{c}^n) - \frac{(\Delta t)^2}{12} \left((J^{2h} \otimes \mathbf{I})^{-1} \tilde{\mathcal{L}}^{2h} \mathbf{c}^{n+1}, (\rho^{2h} \otimes \mathbf{I})^{-1} (J^{2h} \otimes \mathbf{I})^{-1} \tilde{\mathcal{L}}^{2h} \mathbf{c}^n \right)_{2h}. \blacksquare$$

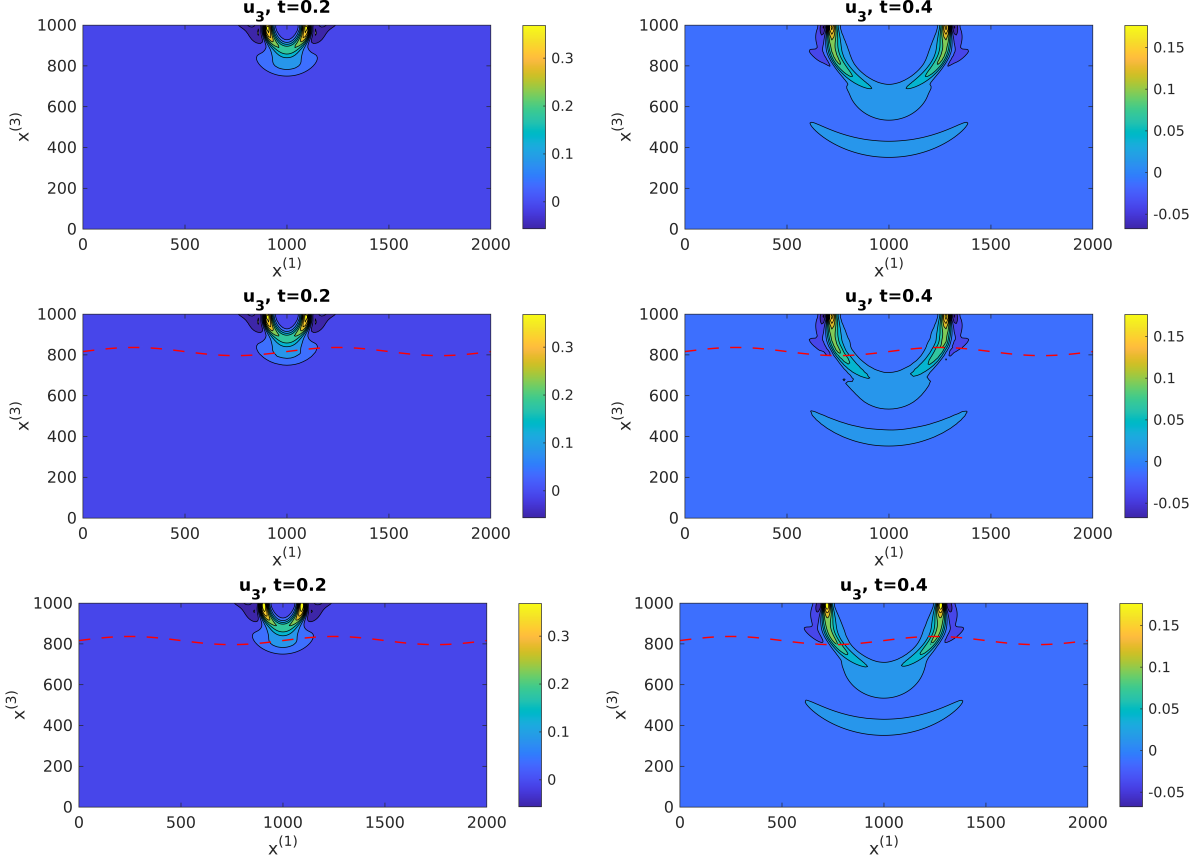


FIG. 7. The graphs for u_3 . In the top, middle and bottom panel, we show numerical solutions at $t = 0.2$ and $t = 0.4$ computed with Mesh 1 (uniform Cartesian grid without any interface), Mesh 2 (curved interface) and Mesh 3 (a refinement of Mesh 2), respectively. The curved interfaces are marked with the red dash lines.

501 We plot the relative change in the fully discrete energy, $(E^{n+1/2} - E^{1/2})/E^{1/2}$, as a function of time with
 502 $t \in [0, 120]$ in Figure 8. This corresponds to 6186 time steps. Clearly, the fully discrete energy remains
 503 constant up to the round-off error.

504 **5.5. LOH.1 model problem with layered material.** As the final numerical example, we consider
 505 the layer-over-halfspace benchmark problem LOH.1 [4]. The computational domain is taken to be
 506 $(x, y, z) \in [0, 30000]^2 \times [0, 17000]$ with a free surface boundary conditions at $z = 0$. The problem is driven
 507 by a single point moment source defined as $g(t, t_0, \omega)\mathcal{M} \cdot \nabla\delta(\mathbf{x} - \mathbf{x}_0)$, where the point source location is
 508 $\mathbf{x}_0 = (15000, 15000, 2000)$ and the moment time function is

$$509 \quad g(t, t_0, \omega) = \frac{\omega}{\sqrt{2\pi}} e^{-\omega^2(t-t_0)^2/2}, \quad \omega = 16.6667, \quad t_0 = 0.36.$$

510 In the 3-by-3 symmetric moment tensor \mathcal{M} , the only nonzero elements are $\mathcal{M}_{12} = \mathcal{M}_{21} = 10^{18}$. The
 511 center frequency is $\omega/(2\pi) = 2.65$ and the highest significant frequency is estimated to be $2.5\omega/(2\pi) =$
 512 6.63.

513 The LOH.1 model has a layered material property with a material discontinuity at $z = 1000$, with
 514 the dynamic and mechanical parameters given in Table 3. In the top layer $z \in [0, 1000]$, both the
 515 compressional and shear velocity are lower than the rest of the domain. For computational efficiency, a
 516 smaller grid spacing shall be used in the top layer.

517 We solve the LOH.1 model problem by using the open source code SW4, where our proposed method
 518 has been implemented. The solution is recorded in a receiver on the free surface at the point $(x, y, z) =$
 519 $(21000, 23000, 0)$. The time history of the vertical, transverse and radial velocities are shown in Figure 9

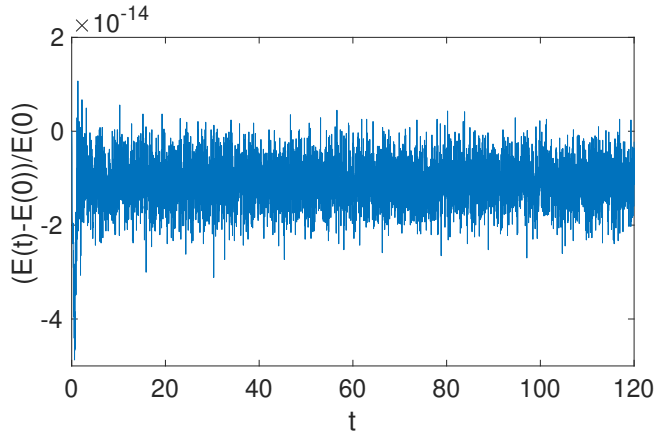


FIG. 8. The relative change in the fully discrete energy as a function of time. Here, $t = 120$ corresponds to 6186 time steps.

	Depth [m]	V_p [m/s]	V_s [m/s]	ρ [Kg/m ³]
Layer	0–1000	4000	2000	2600
half-space	1000–17000	6000	3464	2700

TABLE 3

Dynamic and mechanical parameters for the layer and the lower half-space of the layer over half-space test.

520 with grid spacing $h = 100$ in the half-space and $h/2 = 50$ in the top layer. With the highest significant
 521 frequency 6.63 Hz, the smallest number of grid points per wavelength is only 5.22. Despite this, we
 522 observe the numerical solutions agree well with the exact solution. In Figure 10, the solutions computed
 523 on a finer mesh with $h = 50$ in the half-space and $h/2 = 25$ in the top layer look identical to the exact
 solutions.

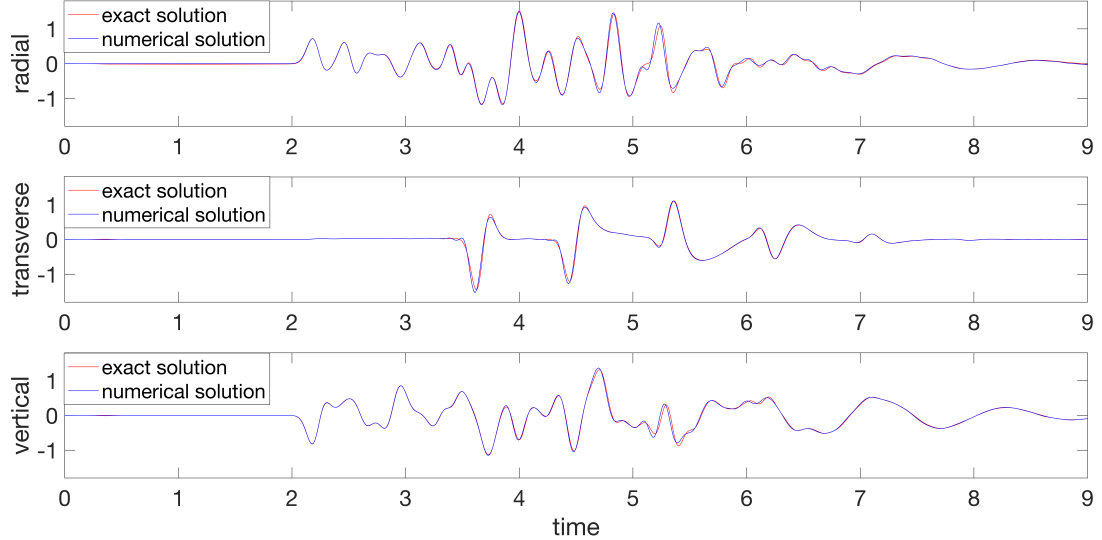


FIG. 9. LOH.1: The radial (top), transverse (middle), and vertical (bottom) velocities time histories. Here the numerical solutions are plotted in blue ($h = 100$) and the semi-analytical solution is plotted in red.

524
 525 To test the performance of the new method, we record the quotient between the computational time
 526 of solving the linear system for the mesh refinement interface and of the time-stepping procedure in Table
 527 4. We have run simulations on two different computer clusters. First, we use two nodes on the Rackham

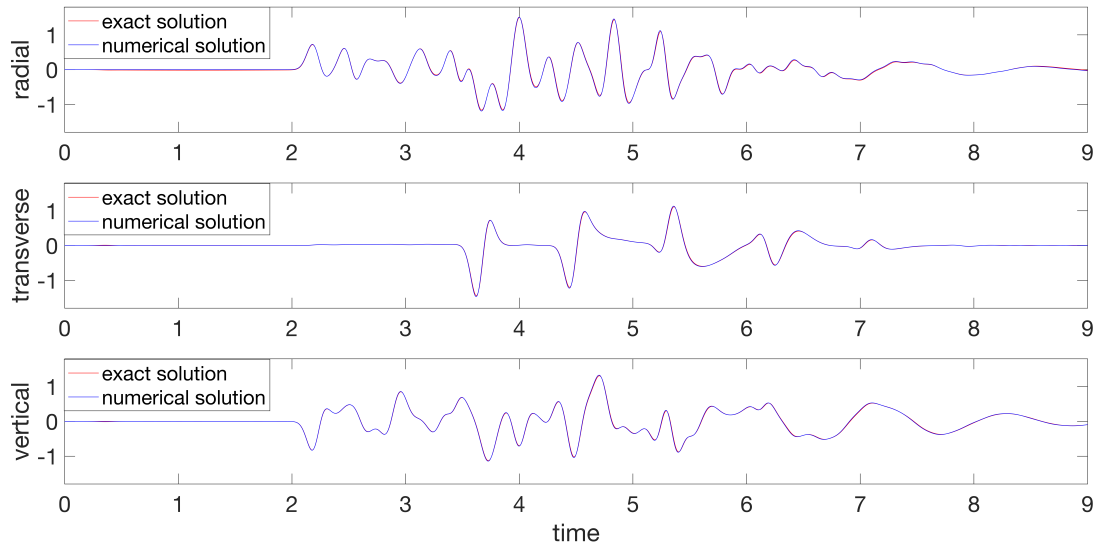


FIG. 10. LOH.1: The radial (top), transverse (middle), and vertical (bottom) velocities time histories. Here the numerical solutions are plotted in blue ($h = 50$) and the semi-analytical solution is plotted in red.

528 cluster with each node consisting of two 10-core Intel Xeon V4 CPUs and 128 GB memory. In the second
 529 simulation, we use three nodes on ManeFrame II (M2) with each node consisting of two 18-core Intel
 530 Xeon E5-2695 v4 CPUs and 256 GB memory. From Table 4, we observe that our new method (with ghost
 531 points from the coarse domain) needs much less time to solve the linear system for interface conditions
 532 compared with the old method in SW4 (with ghost points from both coarse and fine domains).

Machine	new method	old method
Rackham	4.02%	8.16%
M2	5.17%	8.87%

TABLE 4

The quotient of the computational time of solving the linear system for the mesh refinement interface and of the time-stepping procedure

533 In addition, the proposed method implemented in SW4 has excellent parallel scalability. When
 534 running the same model problem with 4 nodes (80 cores) on the Rackham cluster, the computational
 535 time of the time stepping procedure is 51% of that with 2 nodes. Further increasing to 8 nodes (160
 536 cores), the computational time of the time stepping procedure is 52% of that with 4 nodes.

537 **6. Conclusion.** We have developed a fourth order accurate finite difference method for the three
 538 dimensional elastic wave equations in heterogeneous media. To take into account discontinuous mate-
 539 rial properties, we partition the domain into subdomains such that interfaces are aligned with material
 540 discontinuities such that the material property is smooth in each subdomain. Adjacent subdomains are
 541 coupled through physical interface conditions: continuity of displacements and continuity of traction.

542 In a realistic setting, these subdomains have curved faces. We use a coordinate transformation
 543 and discretize the governing equations on curvilinear meshes. In addition, we allow nonconforming mesh
 544 refinement interfaces such that the mesh sizes in each block need not to be the same. With this important
 545 feature, we can choose the mesh sizes according to the velocity structure of the material and keep the
 546 grid points per wavelength almost the same in the entire domain.

547 The finite difference discretizations satisfy a summation-by-parts property. At the interfaces, physical
 548 interface conditions are imposed by using ghost points and mesh refinement interfaces with hanging
 549 nodes are treated numerically by the fourth order interpolation operators. Together with a fourth order
 550 accurate predictor-corrector time stepping method, the fully discrete equation is energy conserving. We
 551 have conducted numerical experiments to verify the energy conserving property, and the fourth order

552 convergence rate. Furthermore, our numerical experiments indicate that there is little artificial reflection
 553 at the interface.

554 To obtain values of the ghost points, a system of linear equations must be solved. In our formulation,
 555 we only use ghost points from the coarse domain, which is more efficient than the traditional approach of
 556 using ghost points from both domains. For large-scale simulations in three dimensions, the LU factoriza-
 557 tion cannot be used due to memory limitations. We have studied and compared three iterative methods
 558 for solving the linear system.

559 Our proposed method has been implemented in the open source code SW4 [15], which can be used
 560 to solve realistic seismic wave propagation problems on large parallel, distributed memory, machines. We
 561 have tested the benchmark problem LOH.1 and verified the improved efficiency.

562 **Acknowledgement.** This work was performed under the auspices of the U.S. Department of Energy
 563 by Lawrence Livermore National Laboratory under Contract DE-AC52-07NA27344. This is contribution
 564 LLNL-JRNL-810518. This research was supported by the Exascale Computing Project (ECP), project
 565 17-SC-20-SC, a collaborative effort of two U.S. Department of Energy (DOE) organizations - the Office
 566 of Science and the National Nuclear Security Administration.

567 Part of the computations were performed on resources provided by Swedish National Infrastructure
 568 for Computing (SNIC) through Uppsala Multidisciplinary Center for Advanced Computational Science
 569 (UPPMAX) under Project SNIC 2019/8-263.

570 **Appendix A. Terms in the spatial discretization.** For the first term in (3.8), we have

$$571 \quad Q_l^{2h}(N_{ll}^{2h})\mathbf{c} := \begin{pmatrix} (Q_l^{2h}(N_{ll}^{2h})\mathbf{c})_1 \\ (Q_l^{2h}(N_{ll}^{2h})\mathbf{c})_2 \\ (Q_l^{2h}(N_{ll}^{2h})\mathbf{c})_3 \end{pmatrix}, \quad (Q_l^{2h}(N_{ll}^{2h})\mathbf{c})_p = \sum_{q=1}^3 Q_l^{2h}(N_{ll}^{2h}(p, q))c^{(q)}, \quad p = 1, 2, 3,$$

573 where we have used a matlab notation $N_{ll}^{2h}(p, q)$ to represent the p -th row and q -th column of the matrix
 574 N_{ll}^{2h} ; $Q_l^{2h}(N_{ll}^{2h}(p, q))c^{(q)}$ is the central difference operator in direction $r^{(l)}$ for spatial second derivative
 575 with variable coefficient. For the second term in (3.8), we have

$$576 \quad \tilde{G}_3^{2h}(N_{33}^{2h})\mathbf{c} := \begin{pmatrix} (\tilde{G}_3^{2h}(N_{33}^{2h})\mathbf{c})_1 \\ (\tilde{G}_3^{2h}(N_{33}^{2h})\mathbf{c})_2 \\ (\tilde{G}_3^{2h}(N_{33}^{2h})\mathbf{c})_3 \end{pmatrix}, \quad (\tilde{G}_3^{2h}(N_{33}^{2h})\mathbf{c})_p = \sum_{q=1}^3 \tilde{G}_3^{2h}(N_{33}^{2h}(p, q))c^{(q)}, \quad p = 1, 2, 3,$$

577 where $\tilde{G}_3^{2h}(N_{33}^{2h}(p, q))c^{(j)}$ is the second derivative SBP operator defined in (3.3) for direction $r^{(3)}$. For
 578 the third term in (3.8), we have

$$580 \quad D_l^{2h}(N_{lm}^{2h}D_m^{2h}\mathbf{c}) := \begin{pmatrix} (D_l^{2h}(N_{lm}^{2h}D_m^{2h}\mathbf{c}))_1 \\ (D_l^{2h}(N_{lm}^{2h}D_m^{2h}\mathbf{c}))_2 \\ (D_l^{2h}(N_{lm}^{2h}D_m^{2h}\mathbf{c}))_3 \end{pmatrix}, \quad (D_l^{2h}(N_{lm}^{2h}D_m^{2h}\mathbf{c}))_p = \sum_{q=1}^3 D_l^{2h}(N_{lm}^{2h}(p, q)D_m^{2h}c^{(q)}), \quad p = 1, 2, 3.$$

582 Here, $D_m^{2h}c^{(q)}$ is a central difference operator in direction $r^{(m)}$ for the spatial first derivative, and $D_3^{2h}c^{(q)}$
 583 is the SBP operator defined in (3.1) for direction $r^{(3)}$.

584 For the second term in (3.10), we have

$$585 \quad G_3^h(N_{33}^h)\mathbf{f} := \begin{pmatrix} (G_3^h(N_{33}^h)\mathbf{f})_1 \\ (G_3^h(N_{33}^h)\mathbf{f})_2 \\ (G_3^h(N_{33}^h)\mathbf{f})_3 \end{pmatrix}, \quad (G_3^h(N_{33}^h)\mathbf{f})_p = \sum_{q=1}^3 G_3^h(N_{33}^h(p, q))f^{(q)}, \quad p = 1, 2, 3.$$

587 Here, $G_3^h(N_{33}^h(p, q))f^{(q)}$ is the SBP operator defined in (3.5) for direction $r^{(3)}$.

588 For the continuity of traction (3.16), we have

$$589 \quad \tilde{\mathcal{A}}_3^{2h}\mathbf{c} = N_{31}^{2h}D_1^{2h}\mathbf{c} + N_{32}^{2h}D_2^{2h}\mathbf{c} + N_{33}^{2h}\tilde{D}_3^{2h}\mathbf{c},$$

590 where

$$591 \quad N_{3l}^{2h}D_l^{2h}\mathbf{c} := \begin{pmatrix} (N_{3l}^{2h}D_l^{2h}\mathbf{c})_1 \\ (N_{3l}^{2h}D_l^{2h}\mathbf{c})_2 \\ (N_{3l}^{2h}D_l^{2h}\mathbf{c})_3 \end{pmatrix}, \quad (N_{3l}^{2h}D_l^{2h}\mathbf{c})_p = \sum_{q=1}^3 N_{3l}^{2h}(p, q)D_l^{2h}c^{(q)}, \quad l = 1, 2, \quad p = 1, 2, 3$$

593 with $D_l^{2h}c^{(q)}$ to be a central difference operator for first spatial derivative in direction $r^{(l)}$, and

$$594 \quad N_{33}^{2h}\tilde{\mathcal{D}}_3^{2h}\mathbf{c} := \begin{pmatrix} (N_{33}^{2h}\tilde{\mathcal{D}}_3^{2h}\mathbf{c})_1 \\ (N_{33}^{2h}\tilde{\mathcal{D}}_3^{2h}\mathbf{c})_2 \\ (N_{33}^{2h}\tilde{\mathcal{D}}_3^{2h}\mathbf{c})_3 \end{pmatrix}, \quad (N_{33}^{2h}\tilde{\mathcal{D}}_3^{2h}\mathbf{c})_p = \sum_{q=1}^3 N_{33}^{2h}(p, q)\tilde{\mathcal{D}}_3^{2h}c^{(q)}, \quad p = 1, 2, 3$$

595

596 with $\tilde{\mathcal{D}}_3^{2h}c^{(q)}$ to be the difference operator for first spatial derivative in direction $r^{(3)}$ defined as in the
597 second equation of (3.4); and

$$598 \quad \mathcal{A}_3^h\mathbf{f} = N_{31}^h D_1^h \mathbf{f} + N_{32}^h D_2^h \mathbf{f} + N_{33}^h D_3^h \mathbf{f},$$

599 where

$$600 \quad N_{33}^h D_3^h \mathbf{f} := \begin{pmatrix} (N_{33}^h D_3^h \mathbf{f})_1 \\ (N_{33}^h D_3^h \mathbf{f})_2 \\ (N_{33}^h D_3^h \mathbf{f})_3 \end{pmatrix}, \quad (N_{33}^h D_3^h \mathbf{f})_p = \sum_{q=1}^3 N_{33}^h(p, q) D_3^h f^{(q)}, \quad p = 1, 2, 3$$

601

602 with $D_3^h f^{(q)}$ to be the SBP operator for first spatial derivative in direction $r^{(3)}$ defined as in the first
603 equation of (3.6). And $N_{3l}^h D_l^h \mathbf{f}$, $l = 1, 2$ are defined similar as those in $\tilde{\mathcal{A}}_3^{2h}\mathbf{c}$.

604 **Appendix B. Bilinear form.** The term $\mathcal{S}_{2h}(\mathbf{c}_t, \mathbf{c})$ in (3.23) is given by

605

$$606 \quad \mathcal{S}_{2h}(\mathbf{c}_t, \mathbf{c}) = (D_1^{2h}\mathbf{c}_t, N_{11}^{2h}D_1^{2h}\mathbf{c})_{2h} + (D_1^{2h}\mathbf{c}_t, N_{12}^{2h}D_2^{2h}\mathbf{c})_{2h} + (D_1^{2h}\mathbf{c}_t, N_{13}^{2h}D_3^{2h}\mathbf{c})_{2h} \\ 607 \quad + (D_2^{2h}\mathbf{c}_t, N_{21}^{2h}D_1^{2h}\mathbf{c})_{2h} + (D_2^{2h}\mathbf{c}_t, N_{22}^{2h}D_2^{2h}\mathbf{c})_{2h} + (D_2^{2h}\mathbf{c}_t, N_{23}^{2h}D_3^{2h}\mathbf{c})_{2h} \\ 608 \quad + (D_3^{2h}\mathbf{c}_t, N_{31}^{2h}D_1^{2h}\mathbf{c})_{2h} + (D_3^{2h}\mathbf{c}_t, N_{32}^{2h}D_2^{2h}\mathbf{c})_{2h} + (D_3^{2h}\mathbf{c}_t, N_{33}^{2h}D_3^{2h}\mathbf{c})_{2h} \\ 609 \quad + (\mathbf{c}_t, P_1^{2h}(N_{11}^{2h})\mathbf{c})_{2hr} + (\mathbf{c}_t, P_2^{2h}(N_{22}^{2h})\mathbf{c})_{2hr} + (\mathbf{c}_t, P_3^{2h}(N_{33}^{2h})\mathbf{c})_{2hr},$$

610 where $P_3^{2h}(N_{33}^{2h})$ is a positive semi-definite operator defined in (3.3) for direction $r^{(3)}$; $P_1^{2h}(N_{11}^{2h})$, $P_2^{2h}(N_{22}^{2h})$
611 are analogue to $P_3^{2h}(N_{33}^{2h})$.

612 The term $\mathcal{S}_h(\mathbf{f}_t, \mathbf{f})$ is defined as

613

$$614 \quad \mathcal{S}_h(\mathbf{f}_t, \mathbf{f}) = (D_1^h\mathbf{f}_t, N_{11}^h D_1^h \mathbf{f})_h + (D_1^h\mathbf{f}_t, N_{12}^h D_2^h \mathbf{f})_h + (D_1^h\mathbf{f}_t, N_{13}^h D_3^h \mathbf{f})_h \\ 615 \quad + (D_2^h\mathbf{f}_t, N_{21}^h D_1^h \mathbf{f})_h + (D_2^h\mathbf{f}_t, N_{22}^h D_2^h \mathbf{f})_h + (D_2^h\mathbf{f}_t, N_{23}^h D_3^h \mathbf{f})_h \\ 616 \quad + (D_3^h\mathbf{f}_t, N_{31}^h D_1^h \mathbf{f})_h + (D_3^h\mathbf{f}_t, N_{32}^h D_2^h \mathbf{f})_h + (D_3^h\mathbf{f}_t, N_{33}^h D_3^h \mathbf{f})_h \\ 617 \quad + (\mathbf{f}_t, P_1^h(N_{11}^h)\mathbf{f})_{hr} + (\mathbf{f}_t, P_2^h(N_{22}^h)\mathbf{f})_{hr} + (\mathbf{f}_t, P_3^h(N_{33}^h)\mathbf{f})_{hr}.$$

618

620 Here, $P_l^h(N_{ll}^h)$ are defined similar as $P_l^{2h}(N_{ll}^{2h})$ in $\mathcal{S}_{2h}(\mathbf{c}_t, \mathbf{c})$.

621 REFERENCES

- 622 [1] M. ALMQUIST, S. WANG, AND J. WERPERS, Order-preserving interpolation for summation-by-parts operators at nonconforming grid interfaces, SIAM J. Sci. Comput., 41 (2019), pp. A1201–A1227.
- 623 [2] M. H. CARPENTER, D. GOTTLIEB, AND S. ABARBANEL, Time-stable boundary conditions for finite-difference schemes solving hyperbolic systems: methodology and application to high-order compact schemes, J. Comput. Phys., 111 (1994), pp. 220–236.
- 624 [3] F. COLLINO, T. FOUCQUET, AND P. JOLY, A conservative space-time mesh refinement method for the 1-D wave equation. Part II: Analysis, Numer. Math., 95 (2003), pp. 223–251.
- 625 [4] S. M. DAY, J. BIELAK, D. DREGER, S. LARSEN, R. GRAVES, A. PITARKA, AND K. B. OLSEN, Test of 3d elastodynamic codes: Lifelines project task 1a01, Technical report, Pacific Earthquake Engineering Center, (2001).
- 626 [5] K. DURU AND E. M. DUNHAM, Dynamic earthquake rupture simulations on nonplanar faults embedded in 3D geometrically complex, heterogeneous elastic solids, J. Comput. Phys., 305 (2016), pp. 185–207.
- 627 [6] K. DURU AND K. VIRTJA, Stable and high order accurate difference methods for the elastic wave equation in discontinuous media, J. Comput. Phys., 279 (2014), pp. 37–62.
- 628 [7] T. HAGSTROM AND G. HAGSTROM, Grid stabilization of high-order one-sided differencing II: second-order wave equations, J. Comput. Phys., 231 (2012), pp. 7907–7931.

- [8] J. E. KOZDON, E. M. DUNHAM, AND J. NORDSTRÖM, Simulation of dynamic earthquake ruptures in complex geometries using high-order finite difference methods, *J. Sci. Comput.*, 55 (2013), pp. 92–124.
- [9] H. O. KREISS AND J. OLIGER, Comparison of accurate methods for the integration of hyperbolic equations, *Tellus*, 24 (1972), pp. 199–215.
- [10] H. O. KREISS AND G. SCHERER, Finite element and finite difference methods for hyperbolic partial differential equations, *Mathematical Aspects of Finite Elements in Partial Differential Equations, Symposium Proceedings*, (1974), pp. 195–212.
- [11] T. LUNDQUIST, A. MALAN, AND J. NORDSTRÖM, A hybrid framework for coupling arbitrary summation-by-parts schemes on general meshes, *J. Comput. Phys.*, 362 (2018), pp. 49–68.
- [12] K. MATTSSON, Summation by parts operators for finite difference approximations of second-derivatives with variable coefficient, *J. Sci. Comput.*, 51 (2012), pp. 650–682.
- [13] O. O'REILLY AND N. A. PETERSSON, Energy conservative SBP discretizations of the acoustic wave equation in covariant form on staggered curvilinear grids, *J. Comput. Phys.*, 411 (2020), p. 109386.
- [14] N. A. PETERSSON AND B. SJÖGREEN, Wave propagation in anisotropic elastic materials and curvilinear coordinates using a summation-by-parts finite difference method, *J. Comput. Phys.*, 299 (2015), pp. 820–841.
- [15] N. A. PETERSSON AND B. SJÖGREEN, User's guide to sw4, version 2.0, Tech. report LLNL-SM-741439, Lawrence Livermore National Laboratory (source code available from <http://geodynamics.org/cig>), (2016).
- [16] B. SJÖGREEN AND N. A. PETERSSON, A fourth order accurate finite difference scheme for the elastic wave equation in second order formulation, *J. Sci. Comput.*, 52 (2012), pp. 17–48.
- [17] B. STRAND, Summation by parts for finite difference approximations for d/dx, *J. Comput. Phys.*, 110 (1994), pp. 47–67.
- [18] J. F. THOMPSON, Z. U. WARSI, AND C. W. MASTIN, Numerical grid generation: foundations and applications, vol. 45, North-holland Amsterdam, 1985.
- [19] S. WANG AND G. KREISS, Convergence of summation-by-parts finite difference methods for the wave equation, *J. Sci. Comput.*, 71 (2017), pp. 219–245.
- [20] S. WANG, A. NISSEN, AND G. KREISS, Convergence of finite difference methods for the wave equation in two space dimensions, *Math. Comp.*, 87 (2018), pp. 2737–2763.
- [21] S. WANG AND N. A. PETERSSON, Fourth order finite difference methods for the wave equation with mesh refinement interfaces, *SIAM J. Sci. Comput.*, 41 (2019), pp. A3246–A3275.